Heliyon 6 (2020) e03773

Contents lists available at ScienceDirect

Heliyon

journal homepage: www.cell.com/heliyon

Research article

MHD effect on mixed convection of annulus circular enclosure filled with Non-Newtonian nanofluid

Emad D. Aboud [a], Hayder K. Rashid [b], Hussein M. Jassim [c], Saba Y. Ahmed [c], Salwan Obaid Waheed Khafaji [c], Hameed K. Hamzah [c], Farooq H. Ali [c,*]

[a] College of Engineering, Al-Musayab-Automobile Engineering Department, University of Babylon, Babylon, Hilla, Iraq
[b] College of Material Engineering, Ceramic Engineering Department, University of Babylon, Babylon, Hilla, Iraq
[c] Mechanical Engineering Department, College of Engineering, University of Babylon, Babylon, Iraq

ARTICLE INFO

Keywords:
Mechanical engineering
Computational fluid dynamics
Nanofluidics
Heat transfer
Magnetohydrodynamics
Computational mechanics
Nanoparticles
Magnetic field
Mixed convection
Annulus circular enclosure
Non-Newtonian fluid
Nanofluid

ABSTRACT

The fluid flow and mixed convection heat transfer of a non-Newtonian (Cu–water) nanofluid-filled circular annulus enclosure in a magnetic field are investigated numerically for a two-dimensional, steady-state, incompressible, laminar flow using the Galerkin finite element method (GFEM). The Prandtl number (Pr = 6.2) and Grashof number (Gr = 100) are assumed to be constants, whereas the Richardson number varies within a range of $0 \leq Ri \leq 1$, the Hartman number within a range of $0 \leq Ha \leq 60$, the Power law index within a range of $0.2 \leq n \leq 1.4$, and the volume fraction within a range of $0 \leq \varphi \leq 1$. The enclosure consists of an outer rotating cylinder that is kept at a cold temperature (T_c) and an inner non-rotating cylinder kept at a hot temperature (T_h). The ratio of the inner circular diameter to the annulus space length is kept constant at 2. The results depict that the stream function increases with increasing power law index, even up to n = 1, which causes the fluid to behave as a Newtonian fluid. The magnetic field has a critical impact on the fluid flow pattern. The average Nusselt number increases with decreasing Richardson number, owing to the improved heat transfer by forced convection.

1. Introduction

The mode of convection heat transfer using a mixture of materials has become a significant process, essentially in numerous households and industrial implementations, heating and cooling of buildings, cooling electronic components, heat exchange systems, and solar energy. This process plays an important role in experimental and theoretical investigations in this field. The behavior of fluid flow and heat transfer have been studied by numerous researchers, and numerous engineering implementations have been conducted. In the recent decade, nanoparticles with high conductivity were proposed as an approach to enhance heat transfer. The dissolution of nanoparticles in the main fluid generates a type of fluid called nano-fluid.

Andreas [1] conducted a theoretical investigation of laminar convection heat transfer to non-Newtonian fluids using some equations for the local Nusselt number. The researchers explored the increasing development of non-Newtonian fluids, such as slushy plastics, pulps, and emulsions. Numerous non-Newtonian fluids have been re-verified for some specific problems in classical hydrodynamics, such as heat transfer in ducts and tubes, pressure decline and flow between eccentric rotary cylinders. The relation between the heat transfer from a vertical chip to a non-Newtonian fluid and the Prandtl number, to determine how the latter affects heat transfer, was studied by Huang et al [2]. The inertia force in the momentum neutralization with the Prandtl number as a finite value was included in their research. The results depicted that the increase in the Prandtl number increased the average heat transfer. The natural convection of identical and incompressible third-grade fluids between two infinite vertical cylinders was investigated by Massoudi et al. [3]. The Influence of a non-Newtonian fluid on the heat transfer and skin friction was supposed. This study presented the effect of using a non-Newtonian fluid on the temperature behavior and velocity for various dimensionless parameters. The finite element method was used by Lockett et al. [4] to analyze the stabilization of non-Newtonian inelastic fluids in a Couette flow using cylinders of infinite length where the inner was rotating. The results presented that the shear-thinning of such a fluid has a considerable influence on the wave and Taylor numbers. The critical aspect ratio was determined for the extensive domain of shear-thinning inelastic fluids. The variance in the critical values was

* Corresponding author.
E-mail address: farooq_hassan77@yahoo.com (F.H. Ali).

https://doi.org/10.1016/j.heliyon.2020.e03773
Received 9 December 2019; Received in revised form 8 February 2020; Accepted 7 April 2020

considered in all the cases and was interesting particularly at a wide annulus. Kimura et al. [5] studied a conjugated convection–conduction, a natural convection from a body in a porous medium saturated with a fluid. The condition of heating was specified in terms of the temperature stability and the distance from the solid porous interface of the solid body surface. The boundary temperature of the solid porous interface of the solid body surface was acquired along with the solution of the temperature domain within the field of interest. Various shapes, such as rectangular panels, thin objects, and horizontal cylinders, were discussed in that study. One-dimensional analysis was conducted to derive the expression for the Nusselt number. The analytical solutions for the time-related processes and the temperature distributions were included for conductive solids.

Khellaf et al. [6] studied numerically the influence of non-Newtonian shear-thinning viscosity modeled by a Carreau-shifted constituent equation. The researchers dealt with the study of mixed natural convection and centrifugal forced convection in a shortened vertical annulus. The inner cylinder was hot and rotating whereas the outer cylinder was cooled and at rest. The required calculations were conducted at various values of the Prandtl number, Weissenberg number, and flow index while retaining the ratio of the height to the gap spacing as well as the radius ratio. The results presented that the friction factor at the rotary cylinder decreases and the heat transfer over the circular gap increases. It was also reported that a reduction in the viscosity, particularly at a forced convection, may cause fluctuating flows. A hot circular cylinder was used for testing an incompressible and non-Newtonian fluid flow of the power-law type by Soares et al. [7]. They evaluated the heat transfer specification when the Reynolds number varied within a range of ($5 \leq Re \leq 40$), power-law index ($0.5 \leq n \leq 1.4$), and the Prandtl number ($1 \leq Pr \leq 10^2$). The results depicted that the influence of n on the flow behavior was high and dependent on the boundary conditions of the cylinder surface and kinematic conditions. A numerical simulation of the flow behavior and the heat transfer mechanization of a non-Newtonian fluid in a circular space between two rotating cylinders was studied by Amoura et al. [8] using the finite element method. The behavior of the rheological fluids was described by the Carreau stress–strain relationship for the inner heated cylinder, which rotated around the same axis with a constant angular velocity while the cooled-external cylinder was fixed. The influence of several parameters, such as the Grashof (Gr), flow index (n), Reynolds (Re), and Weissenberg numbers (We), on the flow behavior and heat transfer was explained. The results presented that there were significant non-Newtonian effects on the heat transfer modes and the flow manner. Concurrently, Abu-Nada [9] studied the improvement of heat transfer depending on the changeable properties of an Al_2O_3water nano-fluid mixture. Variant thermal conductivity and viscosity models were applied to estimate the heat transfer improvement in the annulus. A numerical study on the natural convection of a non-Newtonian nano--fluid flow of two concentric horizontal isothermal cylinders was presented by Matin et al [10]. The governing equations were detached by utilizing the finite volume method-SIMPLE algorithm. The effects of the Prandtl number within a range of (10-10^3) and Rayleigh number (10^3-10^5) on the temperature and velocity were studied for diluted fluids and pseudo-plastic fluids. The average value of the Nusselt number was also studied at different values of the parameters. A reduction in the average Nusselt number was noticed when the power-law index changed from (0.6–1.4). The results depicted that the rate of heat transfer for a false plastic fluid was 170% higher than that for a Newtonian fluid when the value of ($n = 0.6$), whereas it was 43% lower than that for a Newtonian fluid under dilution when the value of ($n = 1.4$). It was noted that as the Rayleigh number increased, the cooling influence of the pseudo-plastic fluid and the insulating influence of the diluted fluid became more notable. An analytical and numerical study on the natural convection of a non-Newtonian nano-fluid flow using two vertical flat plates was presented by Hatami et al [11]. The mixture in this study comprised sodium alginate (SA) as the base non-Newtonian fluid and copper (Cu) with silver (Ag) as the nanoparticles. The viscosity effect was calculated for the nano fluid using the Brinkman and Maxwell–Garnetts (MG) models as well as thermal conductivity. The numerical study included the fourth-order Runge–Kutta numerical method (NUM), least square method (LSM), and differential transformation method to solve the problem. The results depicted that the usage of copper as nano-particles resulted in higher temperature and higher speed of the nano-fluid than with silver, when the Prandtl number increased. An analysis model using the finite difference lattice Boltzmann method to study the influence of a molten polymer on the natural convection of non-Newtonian power-law fluids in a cavity with a sinusoidal heated wall was presented by Kefayati [12]. This research was conducted for a power-law index (n) between (0.5–1.5) and the Rayleigh number (Ra) from (10^4) to (10^5). The results suggested that the finite-difference lattice Boltzmann method was a suitable model for the problem. The increase in n leads to a decrease in the heat transfer, in general. In this research, the usage of a false plastic fluid improved the heat transfer by reducing the power-law index (n) from ($n = 1$) to ($n = 0.5$), so that there was a decrease in the heat transfer when the n increased from 1 to 1.5 in diluted fluids. Kefayati [13] presented a mathematical model based on the finite-difference lattice Boltzmann method to study the influence of a magnetic field on the natural convection of non-Newtonian power-law fluids in a cavity with a sinusoidal heated wall. This research was conducted for a power-law index (n) between (0.5) to (1.5), Rayleigh number (Ra) range (10^4–10^5), Hartman number (Ha) range (0–60), and Prandtl number ($Pr = 10$), whereas the magnetic field was confirmed at various deviations at ($\gamma = 0^\circ$) and ($\gamma = 90^\circ$). The results of this study presented that the increment in (n) in the absence of a magnetic field leads to a decline in the heat transfer. In general, the magnetic field reduced heat transfer at various (n). The increase in the power of the magnetic field reduced the influence of (n) on the heat transfer. The magnetic field for diverse (Ha) at a Rayleigh number of 10^4 demonstrated various influences on the heat transfer versus the increase in (n). When $Ra = 10^5$ and the magnetic field was present, the heat transfer dropped with the raise in (n) as the influence became weak with the increase in (Ha). A numerical simulation using the lattice Boltzmann method to study the natural convection of nano-fluids in a concentric horizontal annulus enclosure was investigated by Fallah et al [14]. A mixture of water as a nano-fluid with nanoparticles of Al_2O_3 was used in their research. In their study, the volume fraction was varied from 0 to 0.04 and the Rayleigh number (Ra) from (10^3) to (10^5). The results proved that the Nusselt number (Nu) increases in the inner and outer cylinders with an increase in the volume fraction and the heat transfer improvement at any (Ra). Kefayati [15] presented an analyzing model for the entropy generation and heat transfer for the laminar natural convection of non-Newtonian nano-fluids in a porous square cavity. Water and nanoparticles, such as of copper (Cu), were loaded in a porous cavity, and the mixture demonstrated shear-thinning behavior. This research was conducted for the specific parameters of the volume fraction (φ) (0–0.04), Darcy number (Da) (0.001–0.1), Rayleigh number (Ra) (10^4–10^5), and power–law index (n) (0.6–1). The results indicated that as the (Ra) increases, the Nusselt number increases. The increase in the volume fraction boosted the entropy generation and heat transfer in accordance to the fluid friction. A decline in (Da) caused the entropy generation and heat transfer to drop highly. A pattern of the free convection boundary layer flow of a non-Newtonian second-stage fluid passed through an impervious isothermal horizontal cylinder was studied mathematically by Ramach and Prasad et al [16]. The dominant boundary layer equations for the momentum, energy, and mass were converted into non-dimensional equations by non-symmetry conversions. In their study, the numerical results were presented for different values of the thermal radiation (R) ranging from (0) to (5), Prandtl number (Pr) ranging from (0) to (100), and Deborah number (De) from (0) to (1.5), and their influence on the temperature profile, velocity profile, Nusselt number (Nu), and shear stress were examined. The results presented that increasing the (Pr) reduces the temperature, flow velocity, and skin friction. A delay in the temperature profiles, flow velocity, and

skin friction was noticed when the radiation parameter increased. A remarkable promotion in (Nu) occurred when there was an increase in (Pr) and the radiation parameter; however, the Deborah number (De) decreased.

Baranwal et al. [17] numerically investigated the laminar free convection heat transfer in power-law fluids in the two-dimensional flow mode for a square duct used for trapping two cylinders side-by-side. The first one was cold, and the other cylinder was hot. The value of the cylinder radius-to-size of the encirclement area (R/L) was fixed at a value of 0.2. The influence of the geometries of the cylinders (value of δ) on the resulting velocity and temperature domains in the laminar free convection mode via considering six similar sites for two cylinders was presented. This work was based on a set of conditions and constants for certain parameters of heat transfer, such as the Prandtl number (Pr) range (0.7–100), Grashof number (Gr) range (10–10^5), power-law index (n) range of (0.3–1.8), Rayleigh number range (7–10^7), and the relative positions of the cylinders in accordance to the centerline (-0.25–0.25). The heat transfer parameters were analyzed in the form of the local Nusselt number over the surfaces of the cylinders and encirclement walls. In general, the average Nusselt number presented a positive adoption of (Gr) and (Pr) regardless of the relative positioning of the cylinders and the (n) values. If the two cylinders were located near the bottom wall, the rate of heat transfer boosted with the signal to that for the symmetrical scenario of the cylinders over the horizontal middle plane of the encirclement. A square cavity filled with an Al_2O_3water non-Newtonian nano-fluid was analyzed numerically by Nazari et al [18]. The two vertical sides of the boundaries of the square were preserved for adiabatic boundary conditions. This study accomplished two cases. In the first case, the right and left side walls were moved vertically at a steady velocity (V_b) in opposite directions. In the other state, the trends of their movements were inverted. The transmission equations were numerically resolved by the finite volume method. The Ostwald-de Waele model for the shear-thinning nano-fluid, which was used by Kefayati [23], was used to calculate the shear stresses with increase in the nano-fluid thermal conductivity. The study included nanoparticles and fluid flow fluctuation by considering the Richardson number and the volume fraction effects. For the second case of this study, the increase in the volume fraction of the nanoparticles increased the heat transfer. The computations in this study were achieved at a constant Grashof number (Gr = 10^5). For the two cases, the results displayed improvement in the heat transfer with increasing nanoparticles volume fraction with a low (Ri).

Kiyasatfar [19] analytically studied a fully developed laminar flow by employing a non-linear slip boundary condition. The analytical study was also designed to include the dissipation of viscosity, locked shape resolution of the velocity profiles, entropy generation rate, Nusselt number (Nu), temperature distributions, and Bejan number (Be) in terms of various factors, such as the power-law index, slip coefficient, and Brinkman number (Br). The results depicted that a decrease in the average entropy generation rate and an increase in (Nu) occurred because of the increase in the slip coefficient. The influence of the slip coefficient on (Be) was highly influenced by (Br). The tendency of (Nu) decreased with (n) and (Br). With dilatant fluids, the influence of (Br) became larger. An increase in (Nu) resulted in an increase in the slip coefficient, but the entropy generation rate decreased. The results proved that microfluidic devices could be more effective with the decrease in the entropy generation rate at the lowest value of (n) and (Br). Under constant conditions, a circular micro-channel demonstrated a higher (Be) and an excellent tendency to provide lower entropy than a parallel-plate micro-channel.

The above discussed survey of the literature reveals that all the previous studies dealt with the natural convection of Newtonian and non-Newtonian fluids in different shapes, such as square ducts, rectangular wavy enclosures, horizontal cylinders, and two non-rotating concentric cylinders with and without magnetic field. Therefore, there is no study on the mixed convection of non-Newtonian power-law fluids in two concentric cylinders where the outer cylinder is rotating and kept cold at (T_c), whereas the inner cylinder is a non-rotating cylinder and kept hot at (T_h). The ratio of the inner circular diameter to the annulus space length is kept constant and equal to 2. Because the mixed convection under a magnetic field inside a concentric circular annulus has numerous engineering applications, non-Newtonian fluids may be more efficient than Newtonian fluids, particularly for cooling or insulating purposes.

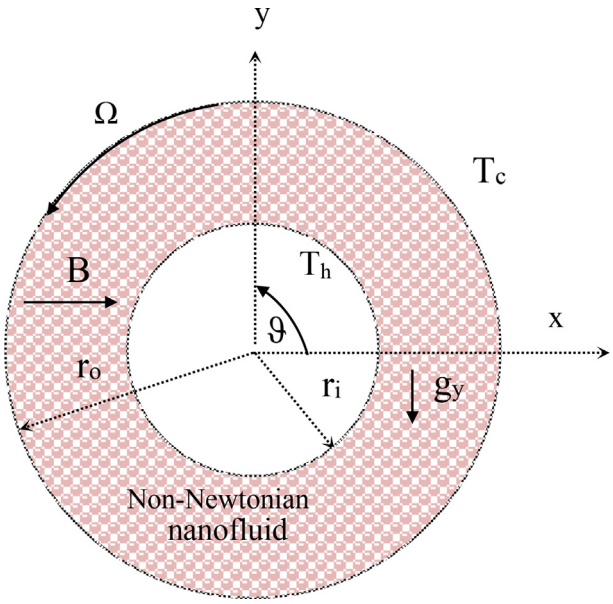

Figure 1. Simplified diagram of the physical system in the present study.

2. Physical model description

The schematic of the present study is presented in Figure 1. The diagram consists of an outer rotating cylinder kept at a cold temperature (T_c) and an inner non-rotating cylinder kept at a hot temperature (T_h). The space between the two cylinders is filled with a non-Newtonian nano fluid. In this study, Cu particles were considered as nanoparticles, and the different thermo-physical solid and liquid properties are listed in Table 1. The ratio between the inner circular diameter ($2r_i$) and the annulus space (r_o-r_i) is kept equal to 2; therefore, the characteristic length is equivalent to the annulus space (r_o-r_i). The liquid phase is represented by water, and the solid phase by the Cu nanoparticles, in the state of thermal equilibrium, and there is no change in the movement between the water and Cu nanoparticles, which have the same magnitude and direction of the flow velocity. Numerous assumptions are considered to simplify the study, such as two-dimensional, steady state, incompressible, and laminar flow. Radiation, Joule heating, and viscous dissipation are factors neglected in this study.

3. Governing equations and boundary conditions

The governing equations in the dimensional form are described as follows for the continuity, momentum in x-direction, momentum in y-direction, and energy [12, 22]:

$$\frac{\partial u}{\partial x}+\frac{\partial v}{\partial y}=0 \tag{1}$$

$$\rho_{na}\left(u\frac{\partial u}{\partial x}+v\frac{\partial u}{\partial y}\right)=-\frac{\partial p}{\partial x}+\left(\frac{\partial \tau_{xx}}{\partial x}+\frac{\partial \tau_{xy}}{\partial y}\right) \tag{2}$$

$$\rho_{na}\left(u\frac{\partial v}{\partial x}+v\frac{\partial v}{\partial y}\right)=-\frac{\partial p}{\partial y}+\left(\frac{\partial \tau_{xy}}{\partial x}+\frac{\partial \tau_{yy}}{\partial y}\right)+g(\rho\beta)_{na}(T-T_c)-\sigma_{na}B_o^2 v \tag{3}$$

Table 1. Thermo-physical properties of water with Cu nanoparticles [25].

Physical Properties	Fluid Phase (Water)	Cu
C_p (J/kg k)	997.1	385
ρ (kg/m^3)	4179	8933
k (W/m k)	0.613	400
β (1/k)	21×10^{-5}	1.67×10^{-5}
μ(kg/ms)	0.000372	-
d_p (nm)	0.385	27
σ (μS/cm)	0.05	5.96×10^{7}

$$\rho c_p\left(u\frac{\partial T}{\partial x}+v\frac{\partial T}{\partial y}\right)=k\left(\frac{\partial^2 T}{\partial x^2}+\frac{\partial^2 T}{\partial y^2}\right) \tag{4}$$

where u and v are the velocity components in the x and y directions, respectively. T is the temperature of the fluid, p is the pressure. Subscript (na) refers to a nanofluid. To transform the governing equation from the dimensional form to a dimensionless form, the following non-dimensional variables are used:

$$X=\frac{x}{r},\ Y=\frac{y}{r},\ U=\frac{Ur}{\alpha},\ V=\frac{vr}{\alpha},\ P=\frac{pr^2}{\mu\alpha},\ \theta=\frac{T-T_c}{T_h-T_c},\ where\ r=r_o-r_i=1 \tag{5}$$

Following the application of the dimensionless parameters mentioned in Eqs. (1), (2), (3), and (4), we obtain the following dimensionless equations:

$$\frac{\partial U}{\partial X}+\frac{\partial V}{\partial Y}=0 \tag{6}$$

$$U\frac{\partial U}{\partial X}+V\frac{\partial U}{\partial Y}=-\frac{\partial P}{\partial X}+\frac{1}{Re}\frac{\rho_{bf}}{\rho_{na}}\frac{1}{(1-\varphi)^{2.5}}\left[2\frac{\partial}{\partial X}\left(\frac{\mu_{bf}}{N}\frac{\partial U}{\partial X}\right)+\frac{\partial}{\partial Y}\left(\frac{\mu_{bf}}{N}\left(\frac{\partial U}{\partial Y}+\frac{\partial V}{\partial X}\right)\right)\right] \tag{7}$$

$$U\frac{\partial V}{\partial X}+V\frac{\partial V}{\partial Y}=-\frac{\partial P}{\partial Y}+\frac{1}{Re}\frac{\rho_{bf}}{\rho_{na}}\frac{1}{(1-\varphi)^{2.5}}\left[2\frac{\partial}{\partial Y}\left(\frac{\mu_{bf}}{N}\frac{\partial V}{\partial Y}\right)+\frac{\partial}{\partial X}\left(\frac{\mu_{bf}}{N}\left(\frac{\partial U}{\partial Y}+\frac{\partial V}{\partial X}\right)\right)\right]+\frac{(\rho\beta)_{na}}{\rho_{na}\beta_{bf}}Ri\theta-\frac{Ha^2}{Re}\frac{\sigma_{na}}{\sigma_{bf}}\frac{\rho_{bf}}{\rho_{na}}V \tag{8}$$

$$U\frac{\partial\theta}{\partial X}+V\frac{\partial\theta}{\partial Y}=\frac{\alpha_{na}}{\alpha_{bf}}\frac{1}{RePr}\left(\frac{\partial^2\theta}{\partial X^2}+\frac{\partial^2\theta}{\partial Y^2}\right) \tag{9}$$

$$\mu_{bf}=N\left\{2\left[\left(\frac{\partial U}{\partial X}\right)^2+\left(\frac{\partial V}{\partial Y}\right)^2\right]+\left(\frac{\partial V}{\partial X}+\frac{\partial U}{\partial Y}\right)^2\right\}^{\frac{(n-1)}{2}} \tag{10}$$

The equations that describe the properties of the nanofluid, such as the density, heat capacity, thermal expansion, thermal conductivity, and effective thermal conductivity [20] can be derived by

$$\rho_{na}=(1-\varphi)\rho_{bf}+\varphi\rho_{sp} \tag{11}$$

$$(\rho c_p)_{na}=(1-\varphi)(\rho c_p)_{bf}+\varphi(\rho c_p)_{sp} \tag{12}$$

$$(\rho\beta)_{na}=(1-\varphi)(\rho\beta)_{bf}+\varphi(\rho\beta)_{sp} \tag{13}$$

$$\frac{k_{na}}{k_{bf}}=\frac{k_{sp}+2k_{bf}+2\varphi(k_{bf}-k_{sp})}{k_{sp}+2k_{bf}-\varphi(k_{bf}-k_{sp})} \tag{14}$$

$$\mu_{na}=\frac{\mu_{bf}}{(1-\varphi)^{2.5}} \tag{15}$$

Eq. (14) represents the thermal conductivity by the Maxwell–Garnetts model, and this model is suitable for spherical nanoparticles and for low temperature gradients [21, 22]. The following equation illustrates the ratio of the electrical conductivity of the nanofluid and the base fluid. The theoretical correlation for the thermal conductivity is given by Eq. (14), electrical conductivity by Eq. (16), and viscosity for the nano-fluid by Eq. (15). These equations help to clarify the anomalous improvement of the properties of the base fluid, such as the thermal conductivity, electrical conductivity. and viscosity.

$$\frac{\sigma_{na}}{\sigma_{bf}}=1+\frac{3\varphi\left(\frac{\sigma_{sp}}{\sigma_{bf}}-1\right)}{\left(\frac{\sigma_{sp}}{\sigma_{bf}}+2\right)-\varphi\left(\frac{\sigma_{sp}}{\sigma_{bf}}-1\right)} \tag{16}$$

A power-law (Ostwald–De Waele) model was applied to the non-Newtonian nanofluid to describe the tensor of the shear stress as follows:

$$\tau_{ij}=2\mu_{na}D_{ij}=\mu_{na}\left(\frac{\partial u_i}{\partial x_j}+\frac{\partial u_j}{\partial x_i}\right) \tag{17}$$

D_{ij} refers to the tensor of rate of deformation in Cartesian coordinates for a steady-state and two-dimensional analysis.

$$\mu_{bf}=N\left\{2\left[\left(\frac{\partial u}{\partial x}\right)^2+\left(\frac{\partial v}{\partial y}\right)^2\right]+\left(\frac{\partial v}{\partial x}+\frac{\partial u}{\partial y}\right)^2\right\}^{\frac{n-1}{2}} \tag{18}$$

where n is the power-law index used to distinguish the fluid type. n = 1 for a Newtonian fluid, such as water, oil, air, glycerol, and alcohol. (n) > 1 for a dilatant, such as corn starch and water (Oobleck), silica, and polyethylene glycol. (n) < 1 for a pseudoplastic, such as likes ketchup, blood, nail polish, paint, and whipped cream.

The dimensionless numbers are classified into constant dimensionless numbers, such as

$$Gr=\frac{g\beta_{bf}r^3(T_h-T_c)}{\nu^2}=100,\ Pr=\frac{\nu}{\alpha}=6.2 \tag{19}$$

whereas the variable dimensionless numbers are

$$Re=\frac{(\omega r_o)r}{\nu_{bf}},\ Ri=\frac{Gr}{Re^2}(0\le Ri\le 1),\ Ha=rB_o\sqrt{\frac{\sigma_{bf}}{\mu_{bf}}}(0\le Ha\le 60) \tag{20}$$

The heat transfer rate is expressed by the local Nusselt number and average Nusselt number, so that

$$Nu_l=\left(\frac{k_{na}}{k_{bf}}\right)\frac{\partial\vartheta}{\partial r} \tag{21}$$

$$\overline{Nu}=\frac{1}{2\pi}\int_1^{2\pi}Nu_l d\vartheta \tag{22}$$

The results of the flow structure are demonstrated by the stream function, which represents the relation between u and v, as specified below.

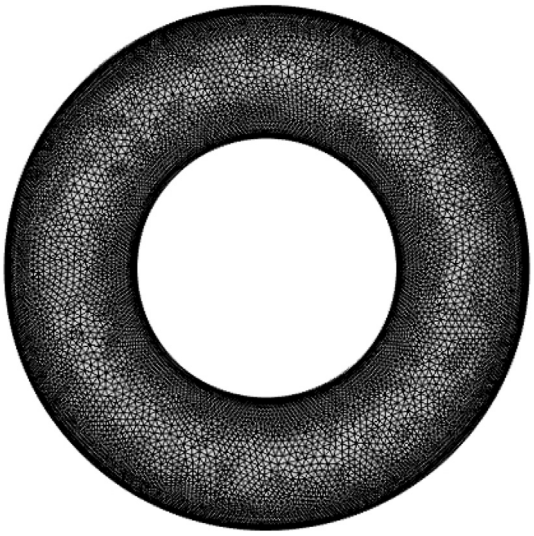

Figure 2. Mesh generation in the present work.

$$U = \frac{\partial \Psi}{\partial Y}, \quad V = -\frac{\partial \Psi}{\partial X} \tag{23}$$

The above relations are combined, and another equation is produced, so that

$$\frac{\partial^2 \Psi}{\partial X^2} + \frac{\partial^2 \Psi}{\partial Y^2} = \frac{\partial U}{\partial Y} - \frac{\partial V}{\partial X} \tag{24}$$

When the flow occurs in a clockwise direction, the stream function is negative. When the flow occurs in an anti-clockwise direction, the stream function is positive. The velocity components around the rotating cylinder are appointed by

$$u = -\omega r_o \sin\vartheta \rightarrow U = -\overline{\omega} R \sin\vartheta \tag{25}$$

$$v = \omega r_o \cos\vartheta \rightarrow V = \overline{\omega} R \cos\vartheta \tag{26}$$

$$\Omega = \sqrt{U^2 + V^2} = \overline{\omega} R \tag{27}$$

where

$$\overline{\omega} = \frac{\omega r^2}{\alpha_{bf}}, \; R = \frac{r_o}{r} \tag{28}$$

The boundary conditions for the present study can be described as the velocity and thermal boundary condition as follows:

On the fixed inner circular cylinder,

$$U = V = \Psi = 0, \; T = T_h \rightarrow \theta = 1 \tag{29}$$

$$\mathrm{U} = -\overline{\omega} R \sin\vartheta, \; \mathrm{V} = \overline{\omega} R \cos\vartheta, \; \Psi = \Psi_c, \; \mathrm{T} = T_c \rightarrow \theta = 0 \tag{30}$$

Ψ_m refers to the mass flow that crosses via any section of the annulus space. It is calculated by the following equation [23, 24, 25].

$$\Psi_c = \left[\int_0^{Y_c or X_c} \left(\frac{\partial \Psi}{\partial Y \; or \; \partial X} \right)_{Y=0 \; or \; Y=0} \right] \tag{31}$$

4. Numerical formulation and code validation

The dimensionless governing Eqs. (6), (7), (8), and (9) and the boundary conditions are solved using the software package, COMSOL Multiphysics, which is an effective environment for the simulation and modeling of all types of scientific and engineering applications based on partial differential equations [28]. The Galerkin finite element method (GFEM) approach is developed to determine the solutions for the governing equations and the boundary conditions of the effect of the MHD on the mixed convection inside an annulus enclosure filled with a non-Newtonian nanofluid. The equation of continuity in dimensionless form (Equation 6) will be utilized as a restraint. This restraint is utilized to calculate the pressure distribution. The resolved dimensionless

Table 2. Grid sensitivity check for volume fractions $\phi = 0.09$ and power-law index $n = 0.6$ at $Ri = 0.001$ and $Ha = 30$.

Mesh size	Mesh elements	Boundary elements	$\overline{Nu}$	CPU time sec	Error
	1344	140	3.4901	5	-
Fine	1878	168	3.3103	6	-5.43
Finer	6406	368	3.1389	10	-5.46
Extra fine	17884	708	3.1620	25	0.73
Extremely fine	20488	708	3.1629	27	0.02

Table 3. Comparison of the average Nusselt numbers from the present and Kefayati's [12, 22] results for different n.

n	Mean Nusselt number at the hot wall, $Ra = 10^4$		Error (%)
	Present study	Kefayati [12]	
0.5	2.9102	2.91	- 0.006
0.7	2.5368	2.53	-0.268
1	2.2374	2.23	- 0.33
1.3	2.0746	2.07	- 0.22
1.5	2.0031	2	-0.155
n	Nu.ave H = 30,Ri = 0.01,ϕ = 0.09		Error %
	Kefayati [22]	Present study	
0.2	5.7776	5.8937	1.9
0.4	6.4814	6.7953	4.6
0.6	8.9584	8.6588	3.4
0.8	9.935	9.9550	0.2
1	10.6409	10.3236	-3.0

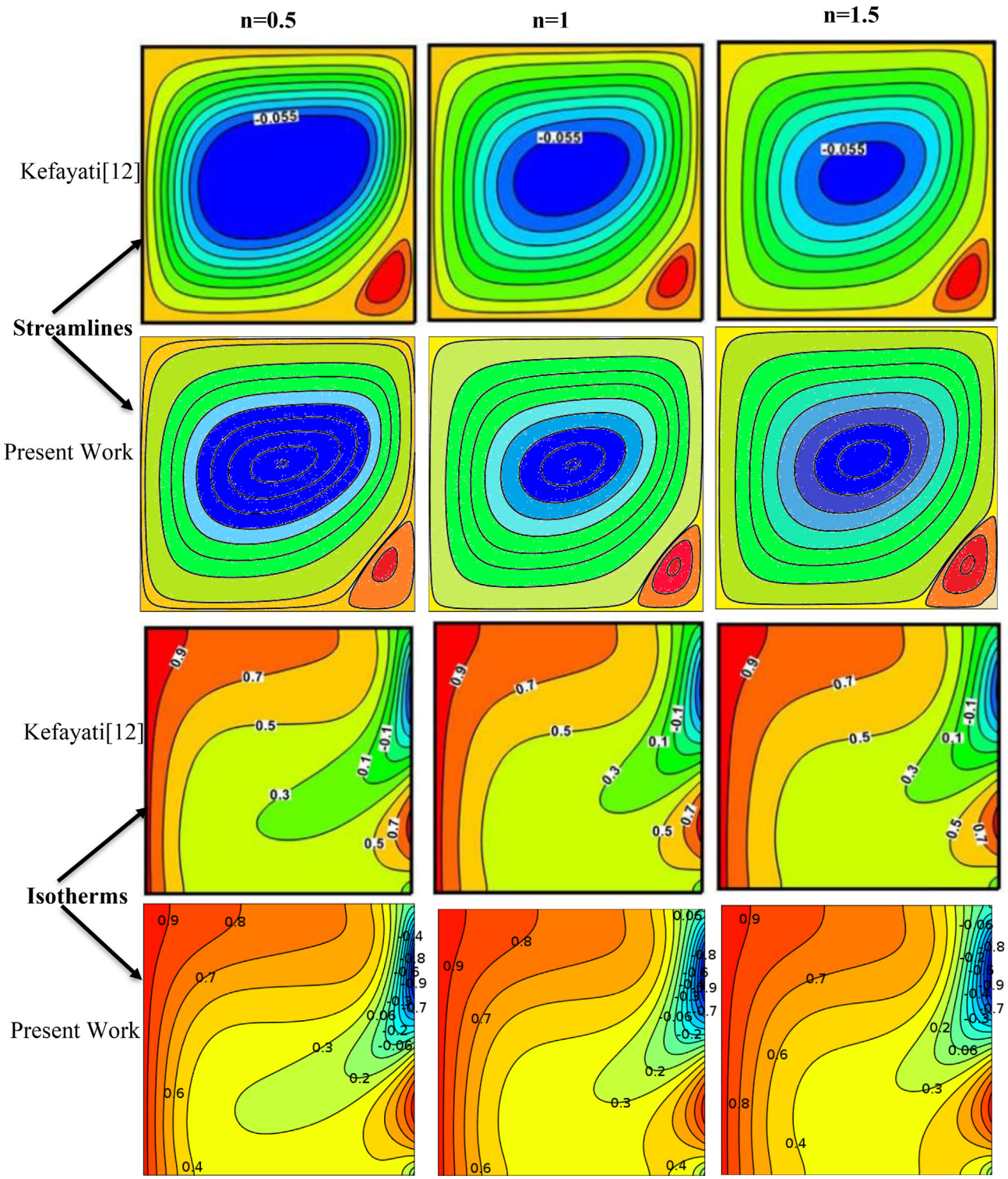

Figure 3. Comparison of the streamlines and isotherms of the present study and Kefayati [12]'s result with Ra = 10^4.

equations are given by Eqs. (7), (8), and (9). The finite element penalty method is utilized, where the pressure term (P) is replaced by a parameter of Penalty (γ). In the present work, the penalty parameter is utilized to deal with the condition of incompressibility (div u = 0). The penalty method has significant consideration in the numerical solution of engineering applications owing to the ability to remove the pressure term from the momentum and eliminating the indefinite parameters. The first step by conveying the continuity equation utilizing the Penalty parameter is

$$P = -\gamma\left(\frac{\partial U}{\partial X}+\frac{\partial V}{\partial Y}\right) \tag{32}$$

Subsequently utilizing Eq. (32), which satisfies the mass conservation equation in the momentum equations, results in

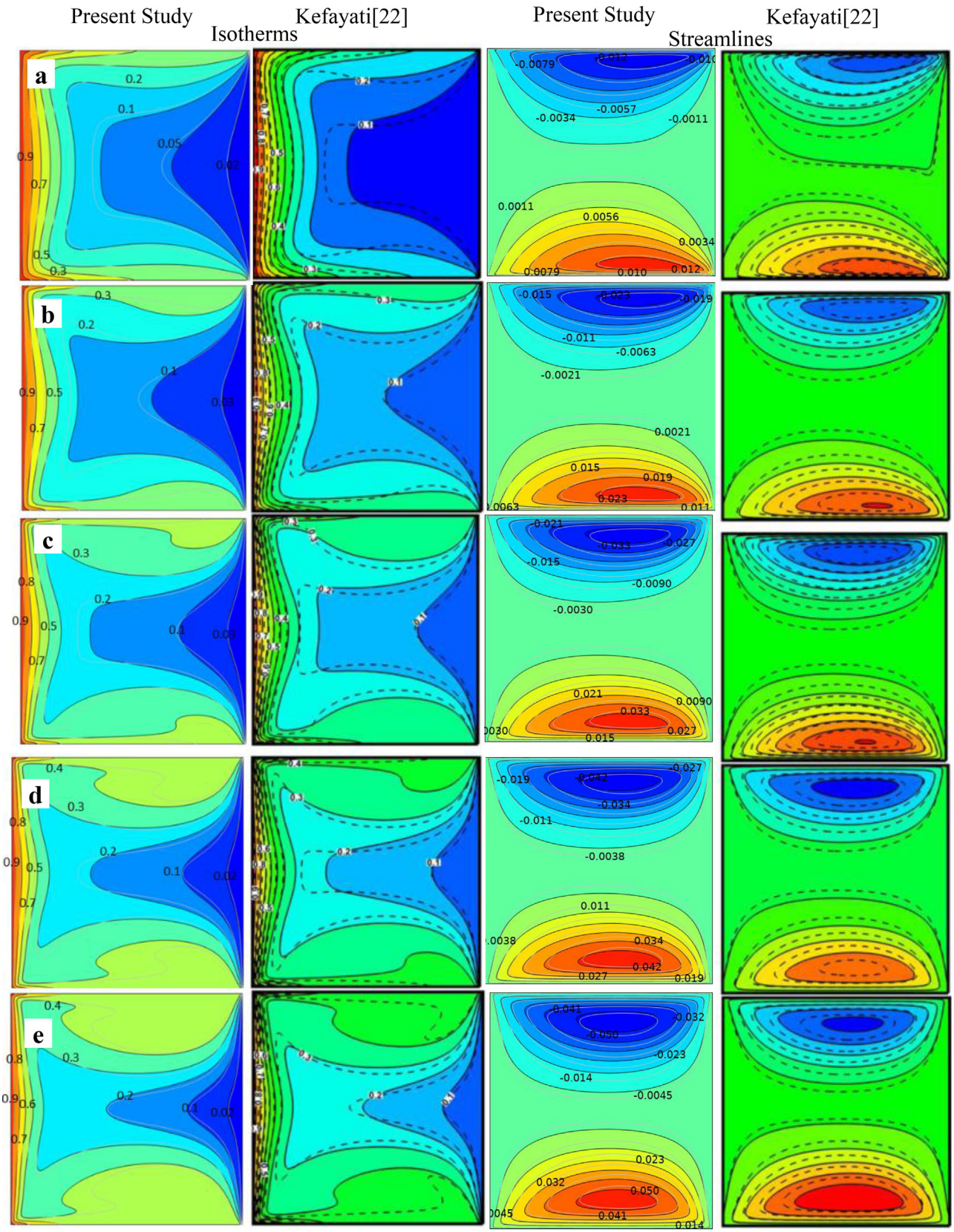

Figure 4. Comparison of the streamlines and isotherms of Kefayati [22] and the present study for various power-law indexes, Ri = 0.01, Ha = 30,ϕ = 0, 0.09, a) n = 0.2, b) n = 0.4, c) n = 0.6, d) n = 0.8, e) n = 1.

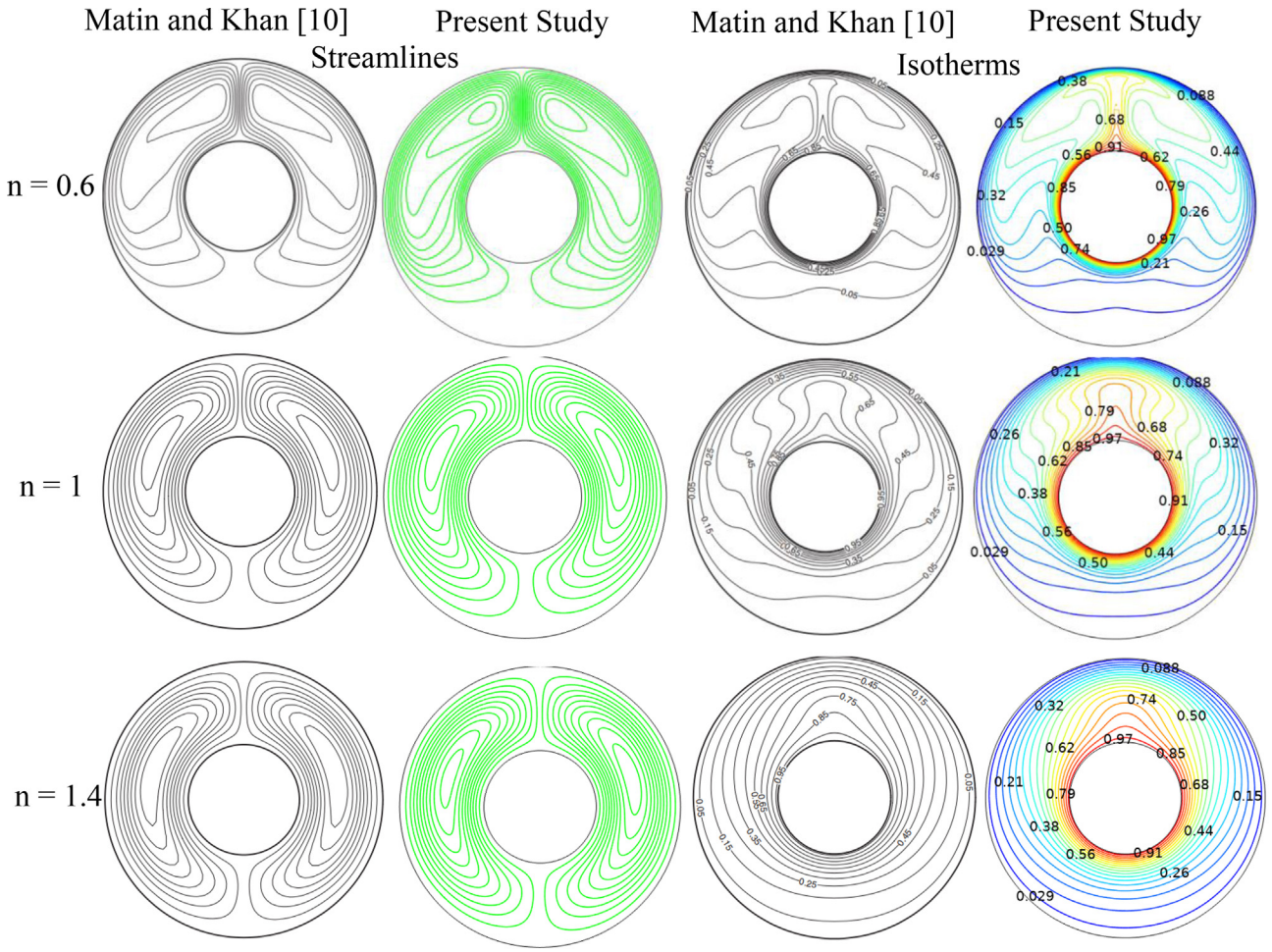

Figure 5. Comparison of the streamlines and isotherms of Matin and Khan [10] and present study for various power-law indices, Pr = 100, Ra = 10^4, and RR = 2.5.

$$U\frac{\partial U}{\partial X}+V\frac{\partial U}{\partial Y}=\gamma\left(\frac{\partial^2 U}{\partial X^2}+\frac{\partial^2 V}{\partial X\partial Y}\right)+\frac{1}{Re}\frac{\rho_{bf}}{\rho_{na}}\frac{1}{(1-\varphi)^{2.5}}\left[2\frac{\partial}{\partial X}\left(\frac{\mu_{bf}}{N}\frac{\partial U}{\partial X}\right)+\frac{\partial}{\partial Y}\left(\frac{\mu_{bf}}{N}\left(\frac{\partial U}{\partial Y}+\frac{\partial V}{\partial X}\right)\right)\right] \tag{33}$$

$$U\frac{\partial V}{\partial X}+V\frac{\partial V}{\partial Y}=\gamma\left(\frac{\partial^2 U}{\partial X\partial Y}+\frac{\partial^2 V}{\partial Y^2}\right)+\frac{1}{Re}\frac{\rho_{bf}}{\rho_{na}}\frac{1}{(1-\varphi)^{2.5}}\left[2\frac{\partial}{\partial Y}\left(\frac{\mu_{bf}}{N}\frac{\partial V}{\partial Y}\right)+\frac{\partial}{\partial X}\left(\frac{\mu_{bf}}{N}\left(\frac{\partial U}{\partial Y}+\frac{\partial V}{\partial X}\right)\right)\right]+\frac{(\rho\beta)_{na}}{\rho_{na}\beta_{bf}}Ri\theta-\frac{Ha^2}{Re}\frac{\sigma_{na}}{\sigma_{bf}}\frac{\rho_{bf}}{\rho_{na}}V \tag{34}$$

The variables (U, V, and θ) utilize the basis set, $\{\Phi_I\}_{I=1}^{M}$, as:

$$U=\sum_{I=1}^{M}U_I\Phi_I(X,\ Y),\quad V=\sum_{I=1}^{M}V_I\Phi_I(X,\ Y)\ and\ \theta=\sum_{I=1}^{M}\theta_I\Phi_I(X,\ Y) \tag{35}$$

The non-linear residual equations produced from Eqs. (9, 33, and 34) following the application of the GFEM approach over the interior nodes of the nodes of the domain (Γ) are

$$R_i^{(1)}=\sum_{I=1}^{M}\theta_I\int_\Gamma\left[\left(\sum_{I=1}^{M}U_I\Phi_I\right)\frac{\partial\Phi_I}{\partial X}+\left(\sum_{I=1}^{M}V_I\Phi_I\right)\frac{\partial\Phi_I}{\partial Y}\right]\Phi_i dXdY-\frac{\alpha_{na}}{\alpha_{bf}}\frac{1}{RePr}\sum_{I=1}^{M}\Phi_I\int_\Gamma\left[\frac{\partial\Phi_i}{\partial X}\frac{\partial\Phi_I}{\partial X}+\frac{\partial\Phi_i}{\partial Y}\frac{\partial\Phi_I}{\partial Y}\right]dXdY \tag{36}$$

$$R_i^{2}=\sum_{I=1}^{M}U_I\int_\Gamma\left[\left(\sum_{I=1}^{M}U_I\Phi_I\right)\frac{\partial\Phi_I}{\partial X}+\left(\sum_{I=1}^{M}V_I\Phi_I\right)\frac{\partial\Phi_I}{\partial Y}\right]\Phi_i dXdY-\gamma\left[\sum_{I=1}^{M}U_I\int_\Gamma\frac{\partial\Phi_i}{\partial X}\frac{\partial\Phi_I}{\partial X}dXdY+\sum_{I=1}^{M}V_I\int_\Gamma\frac{\partial\Phi_i}{\partial X}\frac{\partial\Phi_I}{\partial Y}dXdY\right]-\frac{1}{Re}\frac{\rho_{bf}}{\rho_{na}}\frac{1}{(1-\varphi)^{2.5}}\frac{\mu_{bf}}{N}\left\{\sum_{I=1}^{M}U_I\int_\Gamma\left[2\left(\frac{\partial\Phi_i}{\partial X}\frac{\partial\Phi_I}{\partial X}\right)+\frac{\partial\Phi_i}{\partial Y}\frac{\partial\Phi_I}{\partial Y}\right]dXdY+\sum_{I=1}^{M}V_I\int_\Gamma\left[\frac{\partial\Phi_i}{\partial X}\frac{\partial\Phi_I}{\partial Y}\right]dXdY\right\} \tag{37}$$

$$R_i^{3}=\sum_{I=1}^{M}V_I\int_\Gamma\left[\left(\sum_{I=1}^{M}U_I\Phi_I\right)\frac{\partial\Phi_I}{\partial X}+\left(\sum_{I=1}^{M}V_I\Phi_I\right)\frac{\partial\Phi_I}{\partial Y}\right]\Phi_i dXdY-\gamma\left[\sum_{I=1}^{M}V_I\int_\Gamma\frac{\partial\Phi_i}{\partial Y}\frac{\partial\Phi_I}{\partial Y}dXdY+\sum_{I=1}^{M}U_I\int_\Gamma\frac{\partial\Phi_i}{\partial Y}\frac{\partial\Phi_I}{\partial X}dXdY\right]-\frac{1}{Re}\frac{\rho_{bf}}{\rho_{na}}\frac{1}{(1-\varphi)^{2.5}}\frac{\mu_{bf}}{N}\left\{\sum_{I=1}^{M}V_I\int_\Gamma\left[2\left(\frac{\partial\Phi_i}{\partial Y}\frac{\partial\Phi_I}{\partial Y}\right)+\frac{\partial\Phi_i}{\partial X}\frac{\partial\Phi_I}{\partial X}\right]dXdY+\sum_{I=1}^{M}U_I\int_\Gamma\left[\frac{\partial\Phi_i}{\partial X}\frac{\partial\Phi_I}{\partial Y}\right]dXdY\right\}-\frac{Ha^2}{Re}\frac{\sigma_{na}}{\sigma_{bf}}\frac{\rho_{bf}}{\rho_{na}}\int_\Gamma\left(\sum_{I=1}^{M}V_I\Phi_I\right)\Phi_i dXdY \tag{38}$$

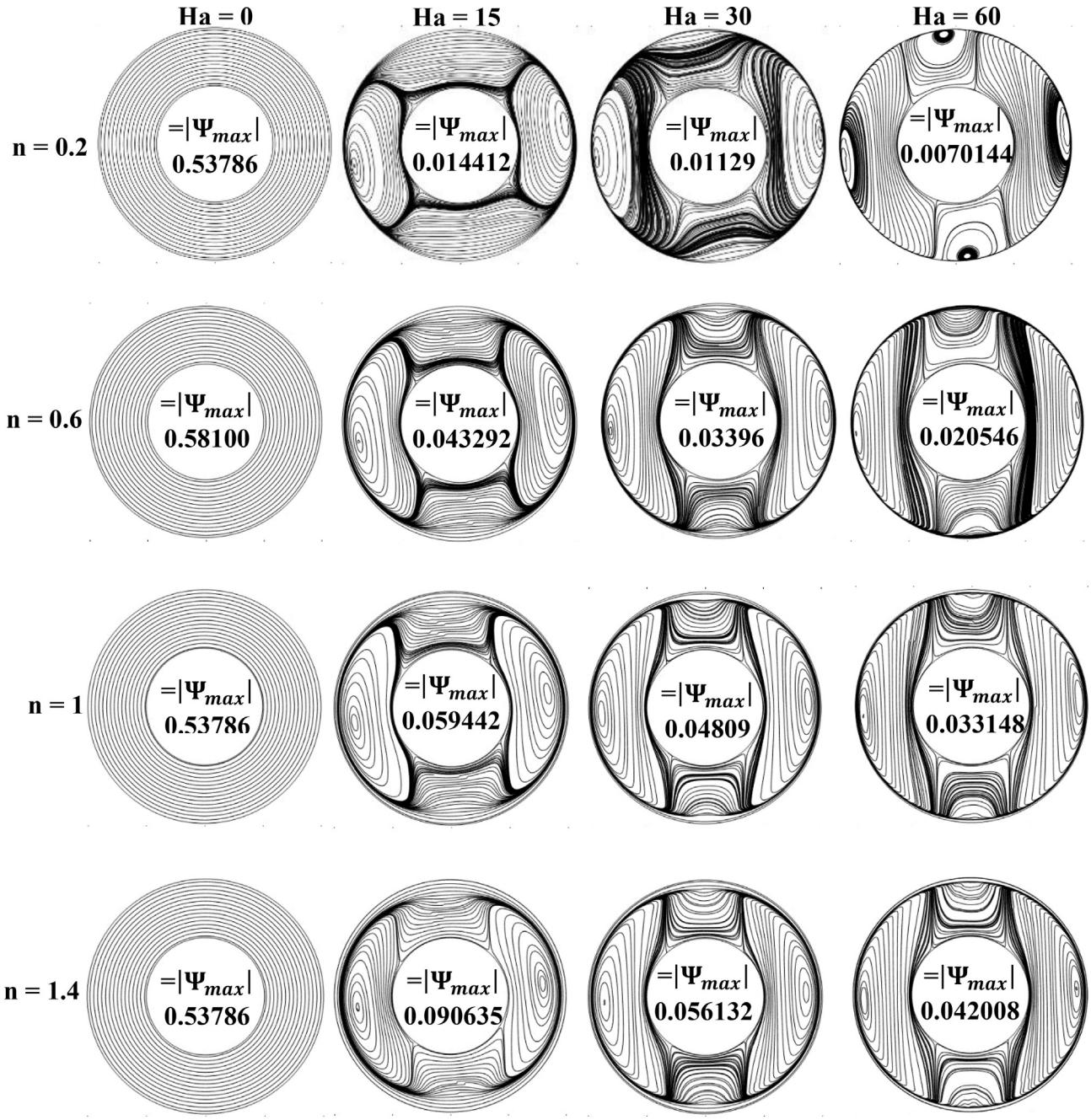

Figure 6. Streamline contours for various power-law indices and Hartmann numbers at Ri = 0.001 and volume fraction (ϕ = 0.09).

Estimating the stream function utilizing the basic function established (Φ as $(\Psi = \sum_{I=1}^{M} \Psi_I \Phi_I(X,Y))$ and Eq. (35) yields

$$R_i^{(4)} = \sum_{I=1}^{M} \Psi_I \int_{\Gamma} \left[\frac{\partial \Phi_i}{\partial X} \frac{\partial \Phi_I}{\partial X} + \frac{\partial \Phi_i}{\partial Y} \frac{\partial \Phi_I}{\partial Y} \right] dXdY + \sum_{I=1}^{M} U_I \int_{\Gamma} \Phi_i \frac{\partial \Phi_I}{\partial Y} dXdY$$
$$- \sum_{I=1}^{M} V_I \int_{\Gamma} \Phi_i \frac{\partial \Phi_I}{\partial X} dXdY \quad (39)$$

For heat transfer, the local Nusselt number along the hot inner wall was calculated from the relation,

$$Nu_I = -\sum_{i=1}^{9} \theta_i \frac{\partial \Phi_i}{\partial n} \quad (40)$$

The basic function of a bi-quadratic has been utilized to estimate indefinite variables, and the process of integration is achieved by the equation of residual using a three-point Gaussian approach. The penalty parameter (γ) is chosen = 10^8; for more details, refer to Ref. [26, 27]. The Newton–Raphson method is used to solve the non-linear equations.

An unstructured triangular element was used to mesh the computational domain. as presented in Figure 2, and a refined mesh was used near the inner and outer walls to obtain accurate results. A grid sensitivity check was achieved to select the suitable element number for the computational numerical study. The checking process was accomplished at φ = 0.09, n 0 = 0.6, Ri = 0.001, and Ha = 30. Four grids were studied: fine (1344 elements), finer (1878 elements), extra fine (17884 elements), and extremely fine (20488). The difference in the average Nusselt number for the grid test is provided in Table 2.

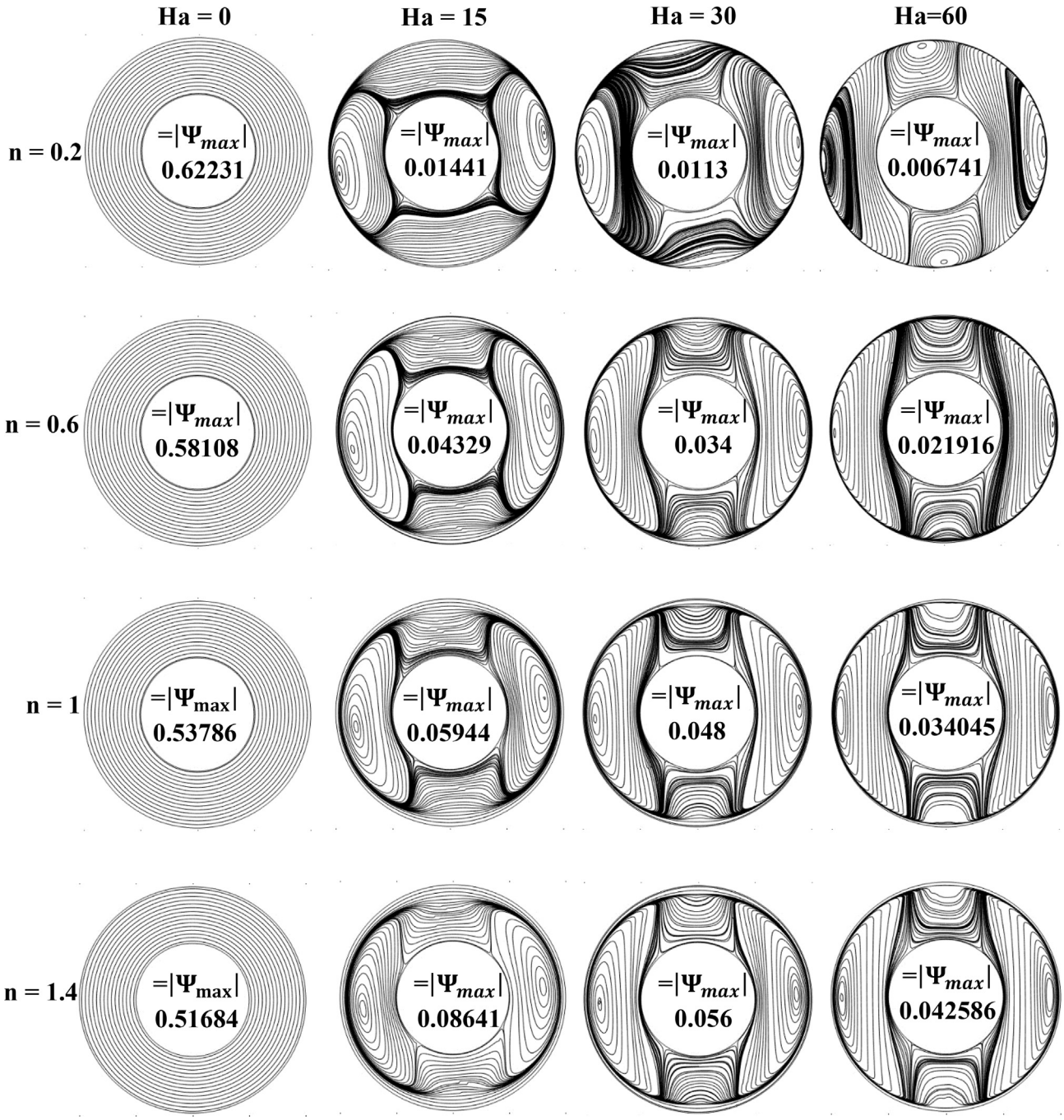

Figure 7. Streamline contours for various power-law indices and Hartmann numbers at Ri = 0.01 and volume fraction (ϕ = 0.09).

The results are validated versus the results of Kefayati [12, 22], who studied the natural convection [12] of a molten polymer non-Newtonian fluid inside a square enclosure under a sinusoidal boundary condition at the right wall. They also studied mixed convection [22] in a square enclosure with a two-sided lid-driven filled with a non-Newtonian fluid under the effect of magnetic field by the finite-difference lattice Boltzmann method. The comparison is performed at Ri = 0.01, Ha = 30, and φ = 0.09. The comparison is obtained for an average Nusselt number and is provided in Table 3. The streamlines and isotherms are presented in Figures 3 and 4. The streamlines and isotherms were also validated against the results of Matin and Khan [10] to obtain high-accuracy results in a concentric cylindrical geometry. Matin and Khan [10] performed a numerical study of the steady-state, two-dimensional natural convection inside a gap between two concentric horizontal cylinders filled with a non-Newtonian fluid, as displayed in Figure 5. The comparison exhibits an excellent agreement between the present study and the published studies by Matin and Khan [10] and Kefayati [12, 22].

5. Results and discussion

In this section, the study of the streamline, contours of isotherms, and average Nusselt number is presented and discussed for different values of the power-law index (n), Hartman number (Ha), and Richardson number (Ri) in detail. The results are summarized only for (φ = 0.09) as the nanoparticle volume fraction, so that the current results might not be valid for another volume fraction, which is out of the scope of this work. The studied parameters are Hartman number $0 \leq Ha \leq 60$, power-law index $0.2 \leq n \leq 1.4$, Richardson number $0.001 \leq Ri \leq 1$, and volume

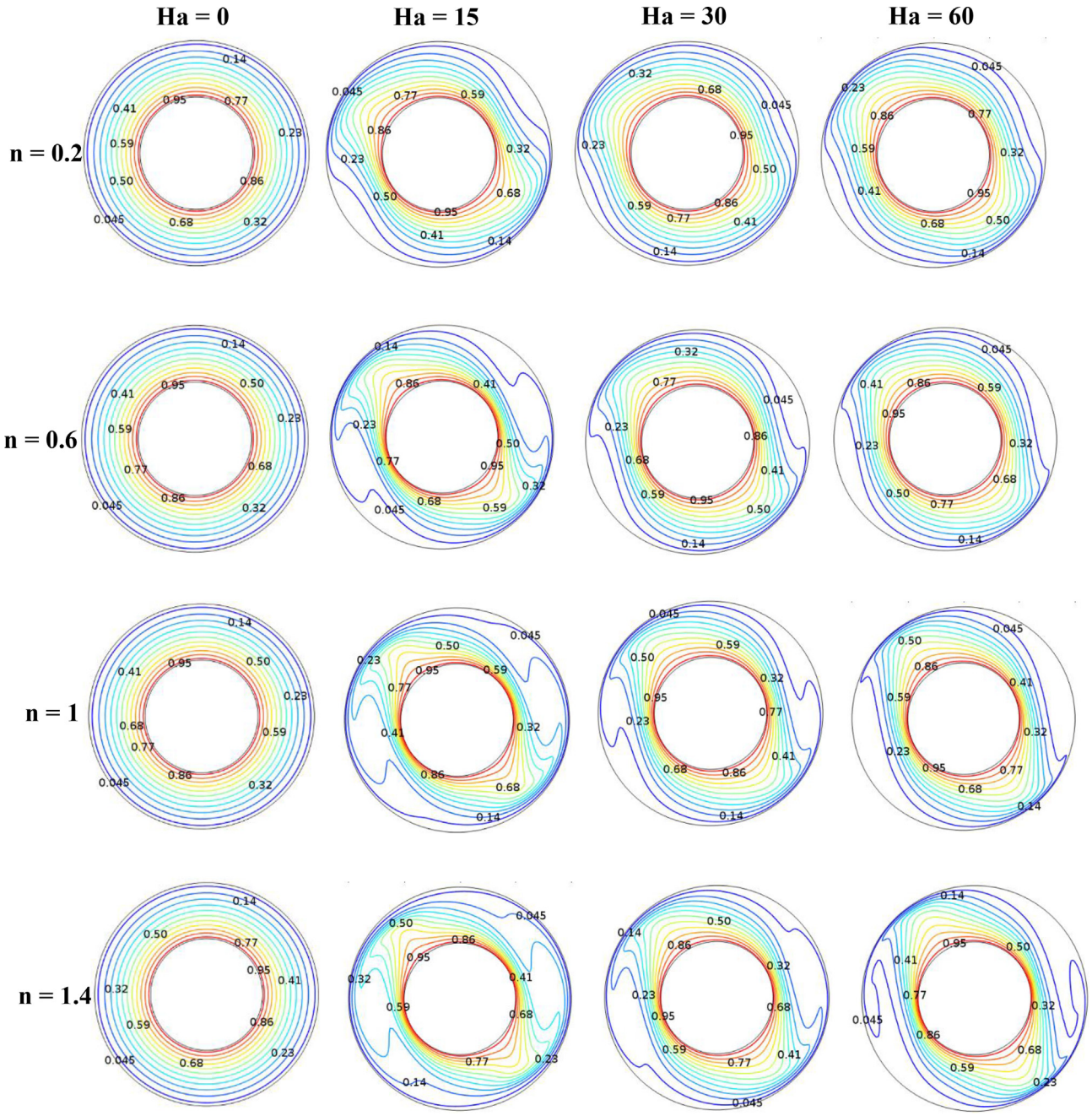

Figure 8. Isotherms for various power-law indices and Hartmann numbers at Ri = 0.001 and volume fraction ($\phi = 0.09$).

fraction percentage $0 \leq \varphi \leq 0.09$, for both the Grashof number (Gr = 100) and the Prandtl number (Pr = 6.2) are assumed to be constant.

Figure 6 presents the effect of the Hartman number on the streamline contours for several values of the power law-index (n) at Richardson number (Ri = 0.001), where the forced convection is dominant for the fluid flow process. In the absence of the magnetic field, as depicted in the first column of Figure 6, uniform circles are generated and presented between the inner and outer cylinders. The circles are driven by the forced convection flow where the buoyancy effect vanishes. The streamlines adopt the shape of the rotating cylinder for all the power-law indices owing to the effect of inertia of the outer rotating cylinder. However, maximum stream function Ψ does not have a noticeable change with the increase in the fluid power-law index (n) because the force of inertia is dominant. It can be noted that the stream function increases with the increase in the power-law index, even to 1, causing the fluid to behave similar to a Newtonian fluid. The trend is no longer the same following the critical value of the power index owing to its non-linear effect, referring to the equation of the power-law index (Equation 18). In addition, a drastic change in the streamline contours is noticed in the presence of a magnetic field, which is represented by the Hartman number. It is known that a magnetic field influences the fluid flow pattern in two independent approaches: modifying the fluid properties and modifying the fluid-flow-driven force. Moreover, a noticeable distortion in the circular forms of the streamlines is recognized in the presence of a magnetic field. For example, at Hartman number (Ha = 15), the streamlines deform to create two main circulations to the left and right of the annulus space. The center of these circulations is very close to the outside wall, which is because the variations in the fluid viscosity are affected by the applied magnetic field. This behavior can be considered as an evidence of the streamline density close to the cold and hot surfaces as presented. At Ha = 15, the surface area of the circulations and the maximum stream function increase with the flow index. However, the

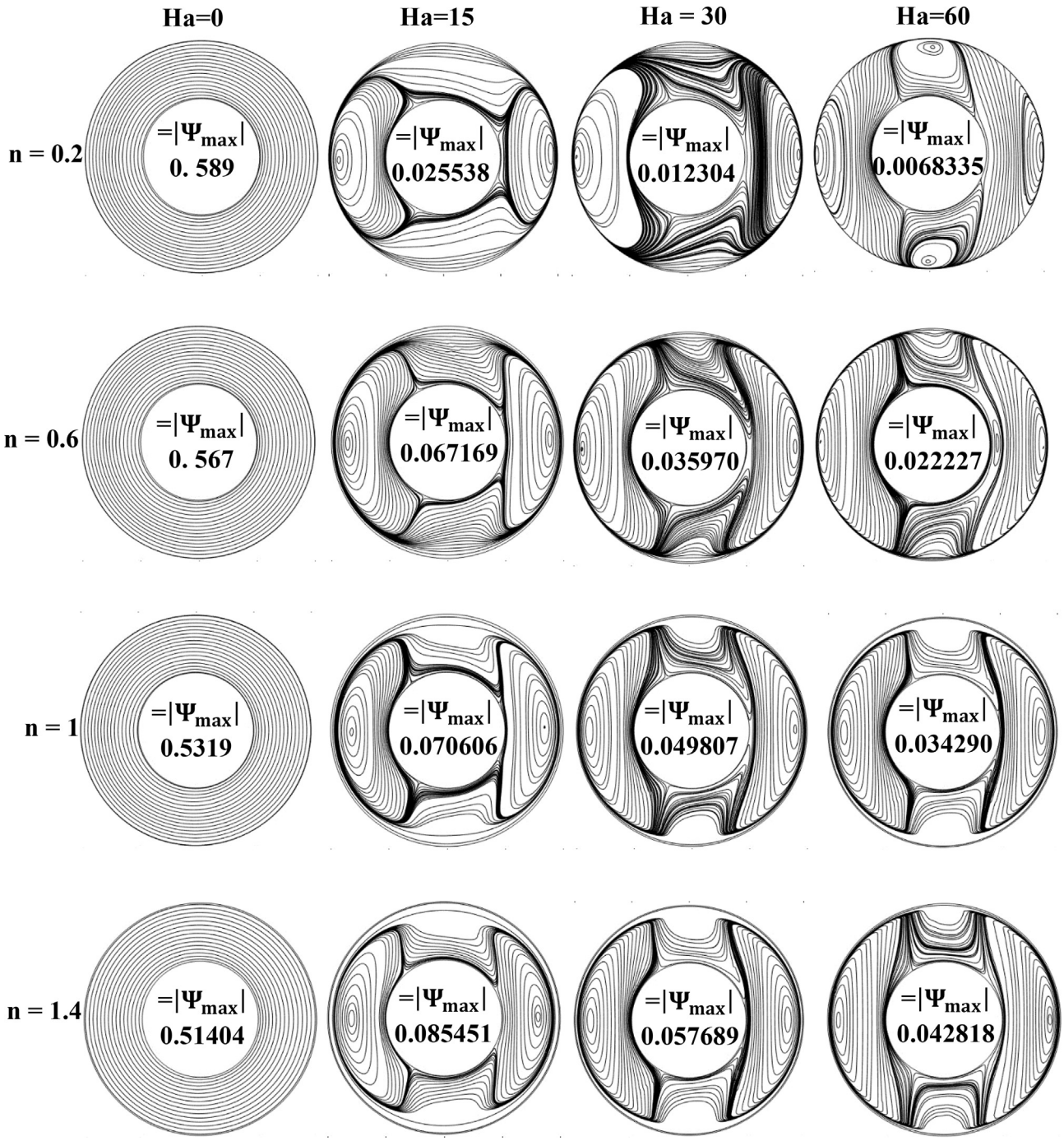

Figure 9. Streamline contours for various power-law indices and Hartmann numbers at Ri = 1 and volume fraction (ϕ = 0.09).

streamline density on the hot surfaces reduces with an increase in the power-law index, owing to the alteration of the fluid behavior. The horizontal direction of the magnetic force has a strong influence on the shape, location, and intensity of the streamline circulation.

A similar streamline can be noticed for the other values of Hartman numbers (Ha = 30 and Ha = 60) when the power-law index varies from 0.2 to 1.4. Moreover, it can be seen that the power-law index not only enhances the stream function but also the heat transfer process, which will be discussed in the next section. As the power-law index increases, the cores of the two circulations move inside to the hot surface at a longer distance from the cold surface. For example, at Ha = 15 and n = 0.2, stream function $|\Psi_{max}| = 0.014412$; as the power-law index (n) increases, the stream function increases and becomes $|\Psi_{max}| = 0.090635$ for n = 1.4. Contrastingly, as the Hartman number increases, the stream function decreases and becomes $|\Psi_{max}| = 0.0070144$ and $|\Psi_{max}| = 0.042008$ at Ha = 60 and n = 0.2, 1.4, respectively. The fluid layers close to the cold surfaces are neither stratified nor stagnant. The core motion leads to a reduction in the thickness of the boundary layer. Increasing the stream function with the power-law index for all the values of Ha is excellent evidence of the explanation above. However, the effect of the power-law index on the stream function decreases with the increase in the magnetic field intensity. This conclusion can be drawn from a simple comparison of the streamline densities on the hot and cold surfaces and the absolute values of the stream functions. For example, the stream function is enlarged almost (0.0906/0.0144) = 9 times, (0.0561/0.011) = 5.6 times, and (0.042/0.007) = 5.714 times for Hartman numbers 15, 30, and 60,

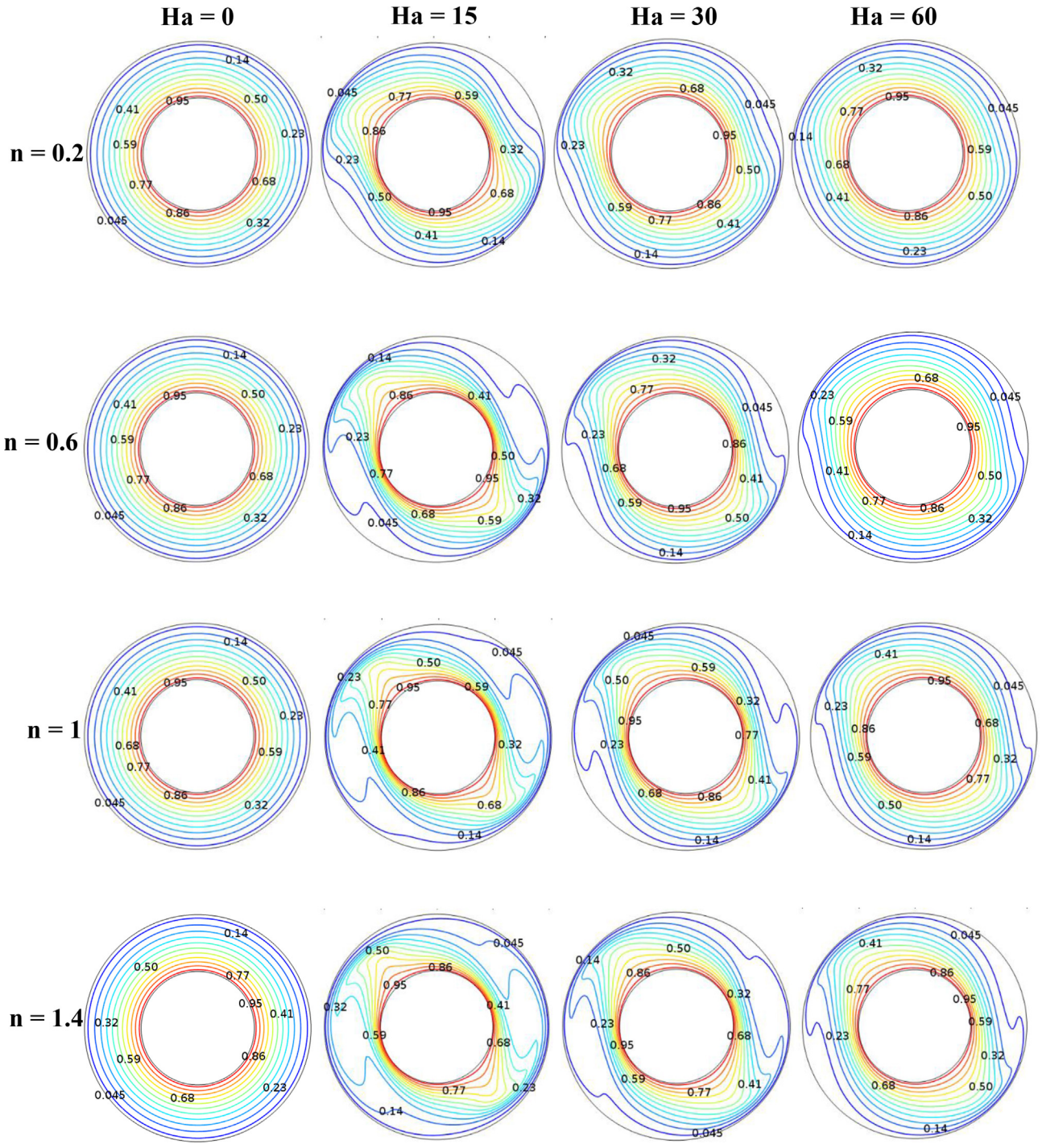

Figure 10. Isotherms for various power-law indices and Hartmann numbers at Ri = 0.01 and volume fraction ($\phi = 0.09$).

respectively. Moreover, for a specific value of the power-law index, the strength of the magnetic field changes the fluid flow behavior by modifying the pattern of the streamline and the stream function values.

In general, the stream function decreases with an increase in the magnetic field strength. For example, when n = 0.2, the stream function reduces 37.34 times when Ha increases to 15 and 47.94 times when Ha increases to 30. The presence of a magnetic field restrains the fluid flow, and thereby, the heat transfer decreases, which will be explained in the next section. However, the more the constraint, the larger the increase in the stagnant regions and stagnant fluid layers. This can be proved by the presence of two circulations at the top and bottom of the cavity close to the cold surface when n = 0.2 and Ha = 60. A similar behavior is noted for other values of n and Ha, and this can be observed easily.

To explain the effect of the Richardson number on the streamline, Figures 6, 8, and 10 are compared. At higher values of Ri, free convection is the dominant process of heat transfer and can be recognized by the presence of the large stagnant area inside the enclosure for the streamlines, and thereby, a large stratified area is developed in the region. However, at the lower values of Ri, force convection is dominant, and higher gradients in the streamline and isotherm are detected. By reducing Ri = 0.01, as presented in Figure 7, no alteration in the general behavior and pattern is noticed. In addition, the isotherm density close to the hot surface decreases dramatically with the increase in Ha, which can be

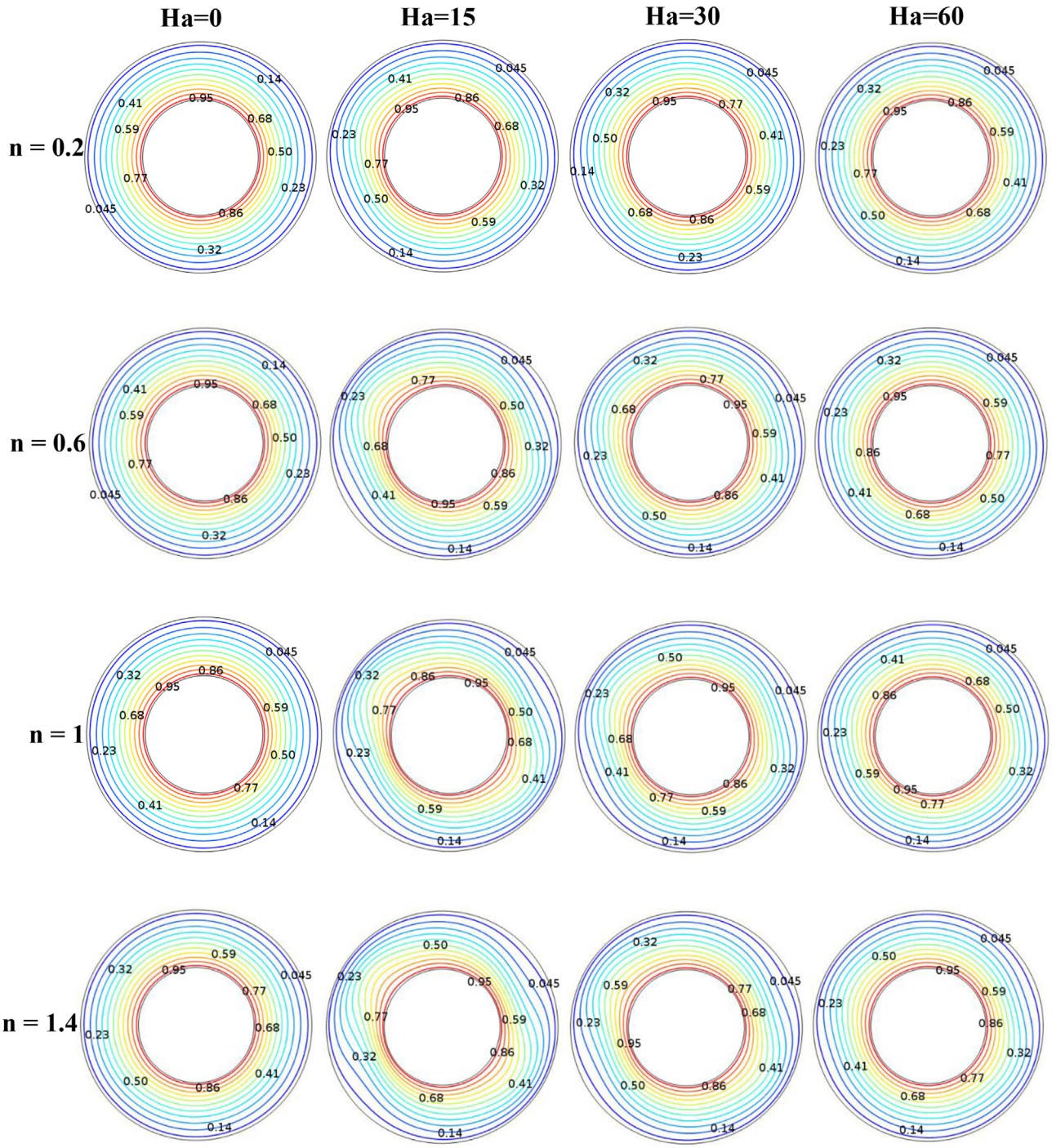

Figure 11. Isotherms for various power-law indices and Hartmann numbers at Ri = 1 and volume fraction ($\phi = 0.09$).

expressed by the behavior of the corresponding isotherm in Figure 8. This confirms the drop in the isotherm gradients close to the hot surfaces (decrease in the transferred heat). In addition, slight changes in the stream functions are observed owing to the increase in Ri from 0.001 to 0.01. This behavior assumes that the viscous force is more dominant than the buoyancy force via this range of Ri variation (0.001–0.01). With further increase in Ri = 1, as presented in Figure 9, the effect of the natural convection increases corresponding to the decrease in the force convection effect, emerging from the movement of the inner cylinder. Relatively significant changes are observed for the streamline and the corresponding isotherm. These changes result from the combined effect of the free and force convections, which are in competition when Ri = 1. As presented in Figure 9, the upper and lower regions start to distort and deform asymmetrically to the right side of the hot surface (hot cylinder), owing to the effects of the buoyancy force and gravity force of the nanoparticles, which comes into play. Moreover, the thickness of the boundary layers is increased with the increase in Ri from 0.01 to 1, which is indicated by the dominant effect of the gravity and viscous resistive forces. It is remarkable that the magnetic field reduces the velocity gradients and stream function for all the values of Ri, where regardless of the value of the Richardson number. However, the rate of the effect is different. Summarizing, under the effect of a magnetic field, the stream function increases with increasing power-law index, whereas its decreases with the increase in the magnetic strength (Hartman number).

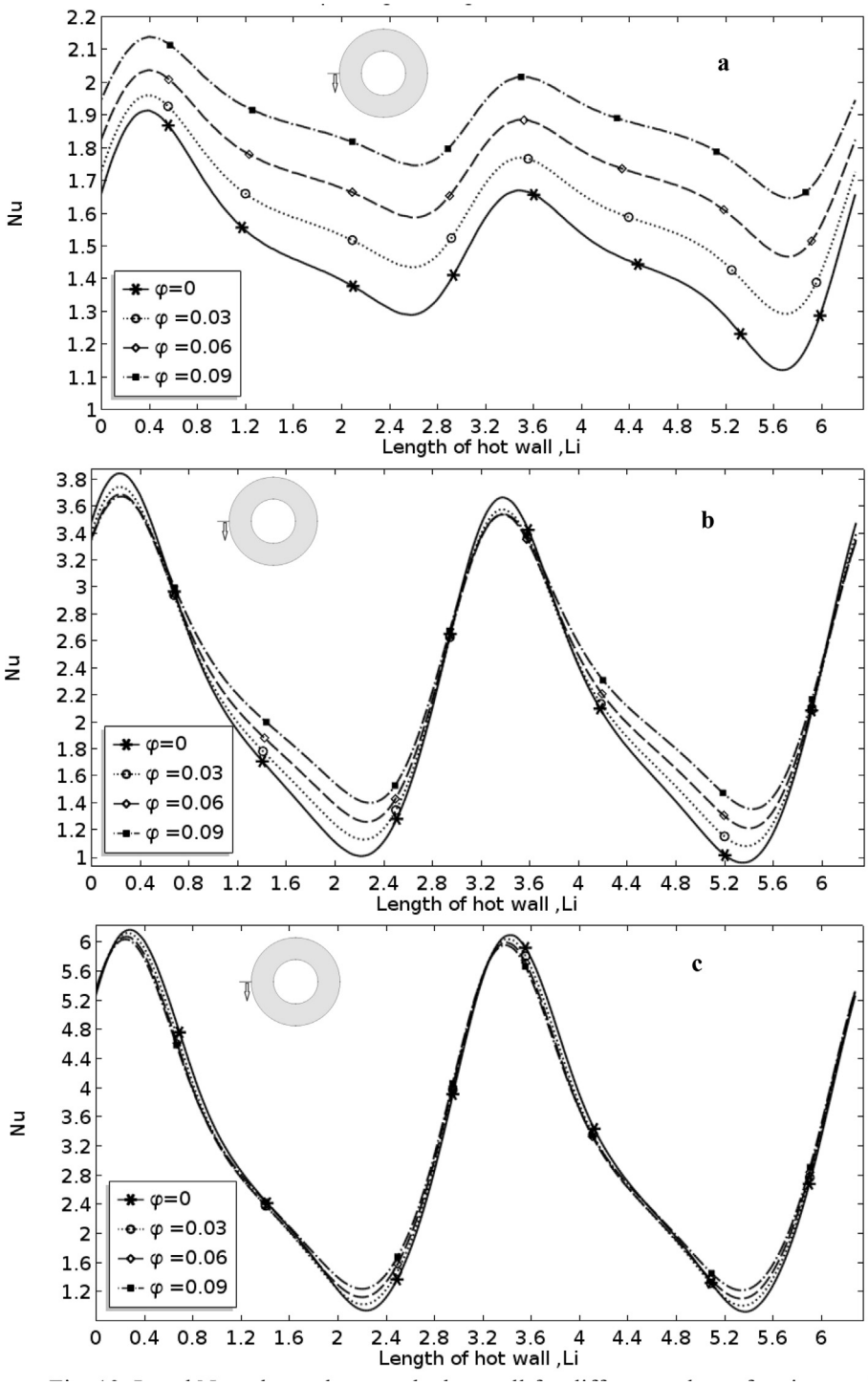

Figure 12. Local Nusselt numbers on the hot wall for different volume fractions and different Richardson numbers at power-law index n = 0.6 and Ha = 30, a) Ri = 1, b) Ri = 0.01, c) Ri = 0.001.

The existence of magnetic force impedes the fluid flow of both a Newtonian fluid (n = 1) and a non-Newtonian fluid (n ≠ 1).

Figures 8, 10, and 11 present the effects of the power-law index and the Hartman number on the heat transfer mechanism and isotherm. In all the figures above, without the magnetic field effect, the isotherms adopt circular shapes, owing to influence of the outer rotating cylinder. Furthermore, the power-law index changes the isotherm pattern in such a way that the isotherm moves toward the cold surfaces and transverses more distance. Temperature gradients increase close to the hot surface, which increases the heat transfer rate. This behavior can be detected by observing the streamline pattern corresponding to the specific figure. Moreover, it is noted that the density of the isotherm (phenomenally enriched) close to the hot surface increases the heat transfer by increasing n. Nevertheless, the isotherm lines become increasingly closer to the hot surface with the increase in index n. However, the isotherm density and its closeness to the wall change with the increase in the Hartman number because of the fluid flow constraint resulting from rope-like fluid volume aligning along the magnetic field lines. This effect increases with the increase in the Hartman number, owing to the increased magnetic field strength. The isotherm gradient decreases significantly at

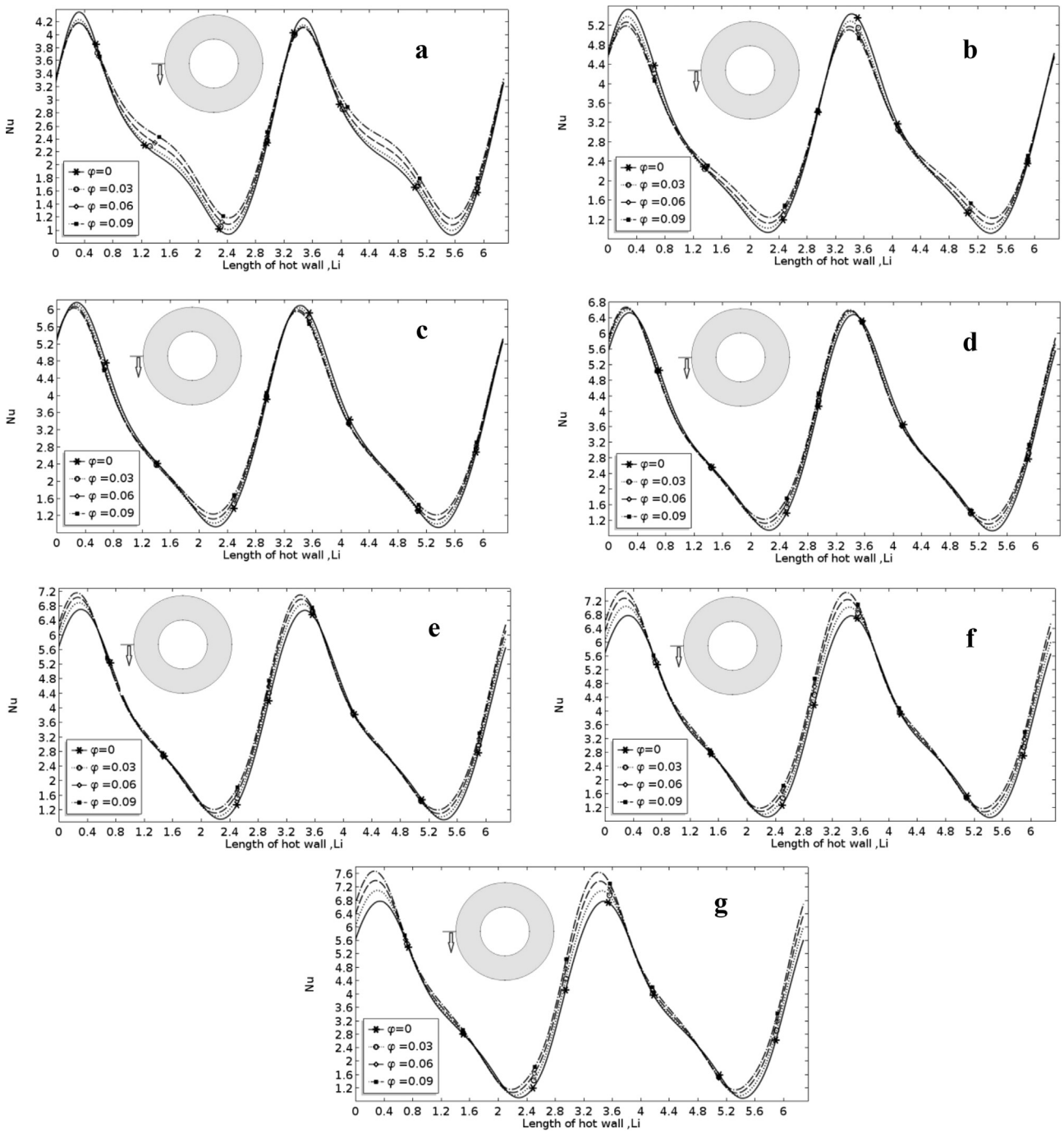

Figure 13. Local Nusselt numbers on the hot wall for different volume fractions and power-law indices at Ri = 0.001 and Ha = 30 a) n = 0.2, b) n = 0.4, c) n = 0.6, d) n = 0.8, e) n = 1, f) n = 1.2, g) n = 1.4.

higher Hartman numbers. It is remarkable that the isotherm density for a specific power-law index decreases at the hot surfaces (inner cylinder) with the increase in the Hartman number. The circular distribution of the isothermal lines vanishes when exposed to a horizontal magnetic field; this behavior leads to a dominant convection heat transfer. When the heat transfer mode changes from conduction (uniform isothermal lines) to convection (non-uniform isothermal lines), an augmentation in the heat transfer rate can observed.

A comparison of Figures 8, 10, and 11 reveals the effect of decreasing the Ri number on the isotherm pattern. A similar behavior can be noticed in Figures 8 and 10 where Ri = 0.001 and Ri = 0.01, respectively. However, the values of the isotherm and the density are slightly different, owing to the increase in the gravity effect. Compared to Ri = 0.001 in Figure 8, the isotherm tendency closer to the hot wall decreases noticeably. Another decrease in the isotherm gradient occurs when the Richardson number increases to 1, as presented in Figure 11, and in general, can be used to confirm the heat transfer, which decreases with the increase in the Ri number. Figure 12 presents the effects of the volume fraction and the Richardson number on the local Nusselt number in the presence of a magnetic field at n = 0.6 and Ha = 30. First, a wavy profile of the local Nusselt number independent of the value of the Ri number is noticed. However, the amplitude of the wavy profile varies with the variation in the Richardson number. The local Nusselt number is calculated from the middle left point, as presented in Figure 12. The peak

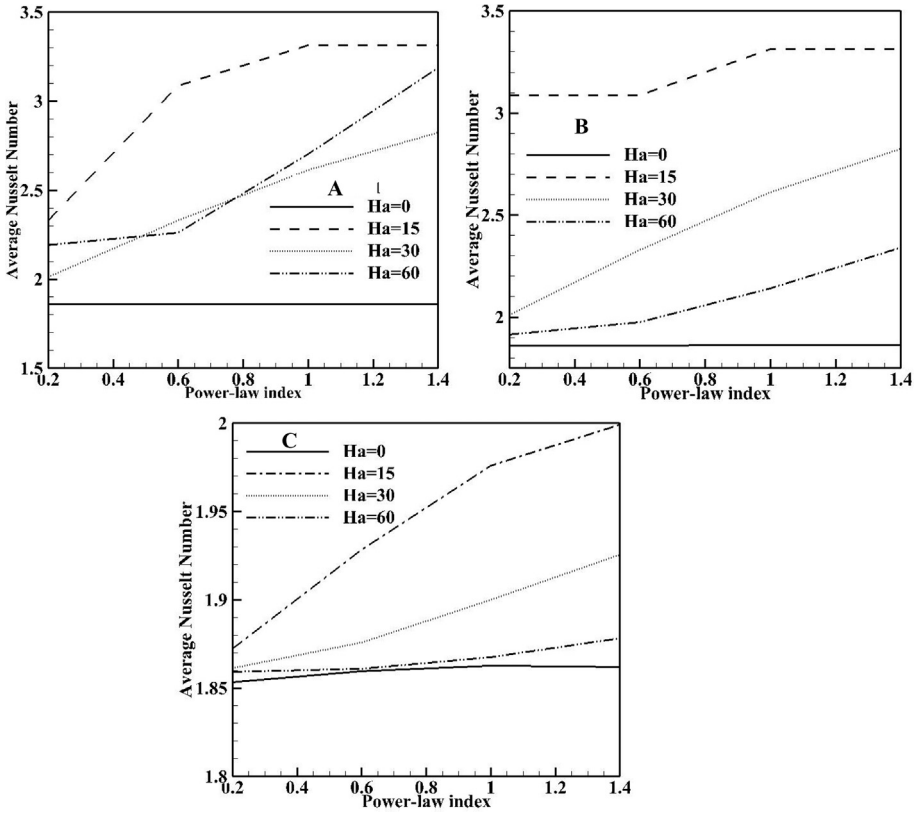

Figure 14. Average Nusselt number versus power-law index for different Richardson and Hartman numbers A) Ri = 0.001, B) Ri = 0.01, C) Ri = 1.

values of the local Nusselt number can be observed at Li = 0.4 ($\vartheta = 0°$) and Li = 3.6 ($\vartheta = 180°$) because of the achievement of a thinner thermal boundary layer. The smallest values of the local Nusselt number can be observed at Li ≈ 2.4 (90°) and Li ≈ 5.6 (270°) because of the achievement of a thicker thermal boundary layer. It is noticed that the local Nusselt number increases with the decrease in the Richardson number from 1 where $(Nu_{loc})_{max} = 2.15$ to 0.001 where $(Nu_{loc})_{max} = 6.1$, because of the domination of the force convection over the free convection. This confirms the variation in the isotherm density on the hot surface at different Ri numbers. It is important to mention that the particle volume fraction plays an essential role in increasing or decreasing the heat transfer rate, as illustrated in the figures above. Particularly for a large Richardson number (Ri = 1), the local Nusselt number for ($\varphi = 0.09$) is the largest among that at all other volume fraction percentages, owing to the thermal conductivity. As the Richardson number decreases, the effect of the nanoparticles vanishes because the inertia force becomes dominant. Generally, increasing the volume fraction increases the fluid viscosity, density, and thermal conductivity. The combined effect of increasing of the three fluid properties is the main reason of the bandwidth (the difference between the maximum and the minimum value of Nu at same length) at different Ri numbers. The Nusselt number increases with the increase in the volume fraction at Ri = 1. However, the trend is reversed when Ri decreases to Ri = 0.01 and Ri = 0.001, owing to the domination of the forced convection at a small Ri number. However, for a small Ri number, the fluid is only driven by the rotational motion of the outer cylinder, i.e., increasing the volume fraction results in increasing the fluid resistance to the flow, owing to the increase in the fluid viscosity. Consequently, this increases the fluid resistivity, which decreases the heat transfer and the corresponding local Nusselt number with increasing volume fraction for Ri = 0.01 and Ri = 0.001, respectively. When Ri = 1, the scenario is different owing to the competition between the free and force convection fluid flows and the manner in which increasing the fluid density, viscosity, and thermal conductivity is going to affect the heat transferred from hot to cold surfaces. Increasing the volume fraction increases the fluid viscosity and density and consequently the fluid flow resistivity, and further decreases the local Nusselt number. However, the corresponding increase in the fluid thermal conductivity effect, owing to the natural convection effect, increases significantly, resulting in recovery of the losses caused by the fluid viscosity and density. Consequently, the local Nusselt number increases as the volume fraction increases at Ri = 1. As can be noticed from Figure 13, the power-law index and the volume fraction affect the local Nusselt number at Ri = 0.001 and Ha = 30. The wavy trend of the local Nusselt number around the hot inner circular cylinder is owing to the difference in the thermal boundary layer thickness around it. The peak value of the local Nusselt number increases with the increasing power-law index because of the heat transfer by the convection becoming stronger. The position of the maximum peak value of local Nusselt number ($Nu_{loc} = 4.3$) at a low power-law index (n = 0.2) is the same as that of ($Nu_{loc} = 7.6$) at (n = 1.4), i.e., Li = 0.3 ($\vartheta = 15°$). In addition, the same trend of the local Nusselt number can be seen for all the power-law index values.

The effect of the magnetic field intensity and the Richardson number on the average Nusselt number is presented in Figure 14. In the three subfigures, the average Nusselt number increases with the decrease in the Richardson number, owing to the enhanced heat transfer by force convection. No significant increment is noticed in the average Nusselt number when Ha = 0 is independent of the value of the power-law index. However, the heat transfer is enhanced in the presence of the magnetic field, as presented notably. The average Nusselt number decreases with Ha, but the trend is different for each value of Ha and the power-law index. The presence of a magnetic field in the fluid layers generates currents in the fluid, which in turn alters its polarization, developing other variations in the magnetic field values. Ropes and chains of the magnetic nanoparticles are generated along the magnetic field lines. The force required to connect the nanoparticles depends on the magnetic field intensity (which is represented by the Hartman number in this study) by the fluid. Owing to the fluid flow (which is represented by the Richardson number in this study), the generated chains deform, extend, and distort.

These alterations depend on the fluid flow strength (Ri) and the magnetic field strength (Ha). The possibility of the deformations, extensions, and distortion increases at lower values of Ha and Ri numbers, which makes the chains and the ropes more flexible. Both the flexibility and fluid flow strength achieve the conditions of fluid potential energy and kinetic energy to be merged and stored, to some extent, between the chains and fluid layers close to the hot surfaces. In a critical scenario following which the flexible chain cannot store more energy before it breaks down, the stored energy will suddenly release, allowing the fluid to flow rapidly close the hot surface, enhancing the heat transfer processes. The combined effect of the Ha and Ri numbers is essential in the process of storing and releasing the energies, and thereby the heat transfer process. The possibility of this process decreases with the increase in Ha, owing to the development of high stiffness in the chains, which makes them harder to deform and break down, which explains the lower values of the Nusselt numbers at higher values of the Ha number.

6. Conclusion

The effect of magnetic field on mixed convection inside an annulus circular enclosure filled with a non-Newtonian-nanofluid (Cu–water) is studied by the Galerkin finite element method (GFEM) at a constant Prandtl number ($Pr = 6.2$) and Grashof number ($Gr = 100$) with Richardson number range ($0.001 \leq Ri \leq 1$), Hartman number range ($0 \leq Ha \leq 60$), power-law index range ($0.2 \leq n \leq 1.4$), and volume fraction range ($0 \leq \varphi \leq 0.09$). The enclosure consists of an outer rotating cylinder that is kept at cold temperature (T_c) and an inner cylinder is non-rotating and is kept at a hot temperature (T_h). The ratio of the inner circular diameter to the annulus space length is kept constant and equal to 2. Very high accuracy results are obtained based on the comparison with a study published previously by Kefayati [22]. The following conclusions can be drawn:

1 Under no magnetic field effect, the stream and isothermal lines have circular shapes for all values of the Richardson number and power low index.
2 At a specific value of the power-law index, the strength of the magnetic field changes the fluid flow behavior by modifying the pattern of the streamlines and stream function values.
3 At $Ha = 15$, the surface area of the circulations and the maximum stream function increase with the flow index.
4 The effect of the power law index on the stream function decreases with the increase in the magnetic field intensity. It can be summarized that the stream function is enlarged 9 times, 5.6 times, and 5.7 for Ha 15, 30, and 60, respectively, which confirms point 1 mentioned above
5 It is observed that the density of the isothermal lines (phenomenally enriched) closer to the hot surface increases the heat transfer by increasing the power-law index, n.
6 At $Ri = 0.01$ and 0.001, the heat transfer and the local Nusselt number decrease with the increase in the volume fraction.
7 The development of the magnetic field strength improves the influence of the nanoparticles on the enhancement of the heat transfer compared with $Ha = 0$.
8 The average Nusselt number increases with the Hartman number, but the trend is different with each value of the Hartman and power law index.
9 The average Nusselt number increases with the decrease in the Richardson number, owing to the enhancement of the heat transfer by the forced convection.

Declarations

Author contribution statement

Emad D. Aboud & Hussein M. Jassim: Contributed analysis tools or data.

Hayder K. Rashid: Contributed analysis tools or data; Wrote the paper.

Saba Y. Ahmed: Conceived and designed the analysis; Wrote the paper.

Salwan Obaid Waheed Khafaji: Analyzed and interpreted the data; Wrote the paper.

Hameed K. Hamzah: Conceived and designed the analysis; Analyzed and interpreted the data.

Farooq H. Ali: Conceived and designed the analysis; Analyzed and interpreted the data; Wrote the paper.

Funding statement

This research did not receive any specific grant from funding agencies in the public, commercial, or not-for-profit sectors.

Competing interest statement

The authors declare no conflict of interest.

Additional information

No additional information is available for this paper.

References

[1] A. Acrivos, A theoretical analysis of laminar natural convection heat transfer to non-Newtonian fluids, AIChE J. 6 (4) (1960) 584–590.
[2] M. Huang, J. Huang, Y. Chou, C.O. Chen, Effects of Prandtl number on free convection heat transfer from a vertical plate to a non-Newtonian fluid, J. Heat Transfer Transcations ASME Am. Soc. Mech. Eng. Series C United States 111 (1) (1989).
[3] M. Massoudi, I. Christie, Natural convection flow of a non-Newtonian fluid between two concentric vertical cylinders, Acta Mech. 82 (1-2) (1990) 11–19.
[4] T.J. Lockett, S.M. Richardson, W.J. Worraker, The stability of inelastic non-Newtonian fluids in Couette flow between concentric cylinders: a finite-element study, J. Non-Newtonian Fluid Mech. 43 (2-3) (1992) 165–177.
[5] S. Kimura, T.O.A.I. Kiwata, A. Okajima, I. Pop, Conjugate natural convection in porous media, Adv. Water Resour. 20 (2-3) (1997) 111–126.
[6] K. Khellaf, G. Lauriat, Numerical study of heat transfer in a non-Newtonian Carreau-fluid between rotating concentric vertical cylinders, J. Non-Newtonian Fluid Mech. 89 (1-2) (2000) 45–61.
[7] A.A. Soares, J.M. Ferreira, R.P. Chhabra, Flow and forced convection heat transfer in crossflow of non-Newtonian fluids over a circular cylinder, Ind. Eng. Chem. Res. 44 (15) (2005) 5815–5827.
[8] M. Amoura, N. Zeraibi, A. Smati, M. Gareche, Finite element study of mixed convection for non-Newtonian fluid between two coaxial rotating cylinders, Int. Commun. Heat Mass Tran. 33 (6) (2006) 780–789.
[9] E. Abu-Nada, Effects of variable viscosity and thermal conductivity of Al2O3–water nanofluid on heat transfer enhancement in natural convection, Int. J. Heat Fluid Flow 30 (4) (2009) 679–690.
[10] M.H. Matin, W.A. Khan, Laminar natural convection of non-Newtonian power-law fluids between concentric circular cylinders, Int. Commun. Heat Mass Tran. 43 (2013) 112–121.
[11] M. Hatami, D.D. Ganji, Natural convection of sodium alginate (SA) non-Newtonian nanofluid flow between two vertical flat plates by analytical and numerical methods, Case Stud. Therm. Eng. 2 (2014) 14–22.
[12] G.R. Kefayati, Simulation of non-Newtonian molten polymer on natural convection in a sinusoidal heated cavity using FDLBM, J. Mol. Liq. 195 (2014) 165–174.
[13] G.R. Kefayati, Simulation of magnetic field effect on natural convection of non-Newtonian power-law fluids in a sinusoidal heated cavity using FDLBM, Int. Commun. Heat Mass Tran. 53 (2014) 139–153.
[14] K. Fallah, A. Ghaderi, N. Sedaghatizadeh, M.H. Borghei, Simulation of natural convection heat transfer using nanofluid IN a concentric annulus, Therm. Sci. 21 (3) (2017).
[15] G.H.R. Kefayati, Heat transfer and entropy generation of natural convection on non-Newtonian nanofluids in a porous cavity, Powder Technol. 299 (2016) 127–149.
[16] V.R. Prasad, R. Bhuvanavijaya, M. Bandaru, Natural convection on heat transfer flow of non-Newtonian second grade fluid over horizontal circular cylinder with thermal radiation, J. Nav. Architect. Mar. Eng. 13 (1) (2016) 63–78.
[17] A.K. Baranwal, R.P. Chhabra, Free convection in confined power-law fluids from two side-by-side cylinders in a square enclosure, Heat Tran. Eng. 37 (18) (2016) 1521–1537.
[18] S. Nazari, E. Akbari, Numerical investigation of non-Newtonian nanofluid mixed convection in a two-opposite direction lid-driven cavity with variable properties, Heat Tran. Asian Res. 48 (2) (2019) 601–623.

[19] M. Kiyasatfar, Convective heat transfer and entropy generation analysis of non-Newtonian power-law fluid flows in parallel-plate and circular microchannels under slip boundary conditions, Int. J. Therm. Sci. 128 (2018) 15–27.
[20] H.C. Brinkman, The viscosity of concentrated suspensions and solutions, J. Chem. Phys. 20 (4) (1952), 571-571.
[21] M.L. Levin, M.A. Miller, Maxwell a treatise on electricity and magnetism, Uspekhi Fizicheskikh Nauk 135 (3) (1981) 425–440.
[22] G.R. Kefayati, FDLBM simulation of magnetic field effect on mixed convection in a two sided lid-driven cavity filled with non-Newtonian nanofluid, Powder Technol. 280 (2015) 135–153.
[23] V.A.F. Costa, A.M. Raimundo, Steady mixed convection in a differentially heated square enclosure with an active rotating circular cylinder, Int. J. Heat Mass Tran. 53 (5-6) (2010) 1208–1219.
[24] J.S. Yoo, Mixed convection of air between two horizontal concentric cylinders with a cooled rotating outer cylinder, Int. J. Heat Mass Tran. 41 (2) (1998) 293–302.
[25] F.H. Ali, H.K. Hamzah, A. Abdulkadhim, Numerical study of mixed convection nanofluid in an annulus enclosure between outer rotating cylinder and inner corrugation cylinder, Heat Tran. Asian Res. 48 (1) (2019) 343–360.
[26] J.N. Reddy, An Introduction to the Finite Element Method, McGraw Hill, New York, 1993.
[27] R. Eid, Higher order isoparametric finite element solution of stockes flow, Appl. Math. Comput. 162 (2005) 1083–1101.
[28] COMSOL MULTIPHYSICS VERSION 5.4. USER'S GUIDE.